

MeqSilhouette : A mm-VLBI observation and signal corruption simulator

Dissertation presented in fulfillment of the requirements for the
degree of
MASTER OF SCIENCE
in the Department of Physics and Electronics
Rhodes University

Author:
Tariq BLECHER
*Department of Physics and
Electronics, Rhodes University*

Supervisors:
Roger DEANE
Gianni BERNARDI
Oleg SMIRNOV
*Department of Physics and
Electronics, Rhodes University*

August 29, 2016

Abstract

The Event Horizon Telescope (EHT) aims to spatially resolve the silhouette (or shadow) of the supermassive black holes in the Galactic Centre (Sgr A*) and M87. The primary scientific objectives are to test general relativity in the strong-field regime and to probe accretion and jet-launch physics at event-horizon scales. This is made possible by the technique of Very Long Baseline Interferometry (VLBI) at (sub)millimetre wavelengths, which can achieve angular resolutions of order $\sim 10 \mu\text{-arcsec}$. However, this approach suffers from unique observational challenges, including scattering in the troposphere and interstellar medium; rapidly time-variable source structure in both polarized and total intensity; as well as non-negligible antenna pointing errors. In this, the first paper in a series, we present the MEQSILHOUETTE software package which is specifically designed to accurately simulate EHT observations. It includes realistic descriptions of a number of signal corruptions that can limit the ability to measure the key science parameters. This can be used to quantify calibration requirements, test parameter estimation and imaging strategies, and investigate systematic uncertainties that may be present. In doing so, a stronger link can be made between observational capabilities and theoretical predictions, with the goal of maximising scientific output from the upcoming order of magnitude increase in EHT sensitivity.

Acknowledgements

Plagiarism

I acknowledge that plagiarism is wrong and hereby declare that the work contained in this document and in the supporting software is my own, save for that which is properly acknowledged.

Tariq Dylan Blecher

The source code for the imaging software package (along with its full development history) accompanying this document is publicly available on the Rhodes University Radio Astronomy Techniques and Technologies software repository at . As such no part of the source code will be printed in this document.

Contents

Abstract	iii
Acknowledgements	iv
Plagiarism	v
1 Introduction	2
1.1 The Event Horizon Telescope (EHT)	4
1.1.1 Scientific opportunities	4
1.1.2 Challenges and obstacles	6
1.1.3 Science extraction : parameter estimation and imaging	6
1.2 Research questions and aims	6
1.3 A realistic mm-VLBI simulator	6
1.4 Outline	8
2 Theory	9
2.1 Radio Interferometry	9
2.1.1 Measurement Equation	9
2.1.2 mm-VLBI observables and data products	9
2.1.3 Variability and the static source assumption	10
2.2 Signal Corruptions	11
2.2.1 Scattering basics	11
2.2.2 Interstellar medium scattering	13
2.2.3 Troposphere	17
2.2.4 Instrumental	22
2.3 A primer on calibration and imaging	25
3 Software implementation	26
3.1 Design objectives	26
3.2 Architechture and Workflow	26
3.2.1 ISM scattering	29
3.2.2 Atmospheric corruption simulator	29
3.2.3 Pointing error simulator	29
3.3 RODRIGUES interface	29
4 Results and analysis	30
4.1 Canonical simulations	30
4.2 A comparison to real data	35

4.3 Calibration and imaging of a time variable source in the presence of the troposphere	35
5 Conclusion	36
Bibliography	40

List of Figures

1.1 The young stellar system HL Tau, observed at 223 GHz by ALMA. The orbits of forming planets appear as dark rings cut out of the disk. The presence of these bodies are surprising given that host star is still very young. The detail in this image was made possible by the milliarcsec resolution achievable with ALMA.	3
1.2 (Image credit: Remo Tilanis) Event Horizon Telescope uses Earth-diameter baselines to attain resolution $\sim 10 \mu\text{arcsec}$	4
2.1 Illustration depicting the basics of scattering in the weak (left) and strong (right) regimes. In the weak regime, the signal is coherently propagated over an area, $A_{\text{weak}} \approx \pi r_F^2$ whereas in the strong regime, coherent propagation is split over many areas of size $A_{\text{strong}} \approx \pi r_0^2$	12
2.2 The λ^2 dependence of scattering kernel size is shown by the solid line. This has been derived from measurements made at $\lambda > 17 \text{ cm}$ [5]. The dotted line shows the derived intrinsic source size which scales as $\lambda^{1.44}$. This was derived from measurements in the wavelength range, $2 \text{ cm} < \lambda < 1.3 \text{ mm}$. The red circles show major-axis observed sizes of Sgr A* and the green points show the derived intrinsic major-axis size. This plot was reproduced from (author?) [12].	14
2.3 Closure phases recorded in a VLBA + LMT observation of Sgr A* at $\lambda = 3.5 \text{ mm}$ [?]. The data points are shown as red circles and blue squares and are only distinguished by the calibrator used. The green envelopes show the 1σ closure phase prediction induced by scattering-induced substructure. Reproduced from ?]	17

2.4 Recorded zenith absorption spectrum in the 160–520 GHz range, taken on Mauna Kea at an altitude of ~ 4000 m. The data has been fit to a sum of H ₂ O lines, an H ₂ O pseudo-continuum and dry absorption lines. The model has been generated using the ATM code, with the bottom panel showing the residuals. Here 'dry' refers to all atmospheric constituents except H ₂ O. Reproduced from (author?) [37]	19
2.5 RMS visibility phase variations versus baseline length for an observation of 1-Jy celestial calibrator 0748 + 240 with VLA in BnA configuration at 22 GHz for 90 min. The open circles show the rms phase as measured whereas the solid squares show these same values with a constant noise term of 10 subtracted in quadrature. showing β changes with distance on the phase screen. Note the three distinct regime but continuous variation in between. The three regimes of the root phase structure function as predicted by Kolomogorov turbulence theory are indicated. Reproduced from ?]	23
3.1 Flow diagram showing basic sequence of a MEQSILHOUETTE simulation pipeline. The specific sequence is determined by the driver script. The details of the station information, observation strategy, tropospheric and ISM conditions are specified in a user-defined input configuration file. The pipeline is extendable, allowing any additional, arbitrary Jones matrices to be incorporated.	28
4.1 An example simulation of ISM scattering towards Sgr A*. The top panel, left to right, shows the original FWHM = 40 μ -arcsec Gaussian (top left), the ISM scattered image on the first night (top middle) and last night (top right) of the observation respectively. The bottom panel, left to right, shows the evolution of the 10 minute-averaged closure phase with epoch (bottom left), uv-tracks for any particular night (bottom middle) and the visibility amplitudes $ V $ of the unscattered (red) and scattered (grey-scale) sources as a function of uv-distance (bottom right). Variations of the flux on the shortest baselines reveal total flux modulation while flux variations $\Delta V $ on longer baselines and non-zero closure phases track the fluctuations in refractive noise. When compared to the latest published observations of Sgr A* [13], we see that the observed and simulated closure phase variability are consistent. Furthermore, ISM scattering simulations can constrain the variability fraction associated with the screen, enabling a more robust estimation of source variability.	31
4.2 Best fit opacity (red) and sky brightness temperature (blue) line solutions at $\nu = 230$ GHz as a function of precipitable water vapour (PWV) for three indicative ground pressures and temperatures which approximately represent the sites of SPT (solid), ALMA (diamond) and SMA (dashed). The legend shows the estimated input ground (pressure, temperature) parameters for each site.	32

4.3	Simulation of the total delay (left) and the turbulent atmospheric delay (right) for SMA (blue) and ALMA (green) sites towards Sgr A*. Ground pressures and temperatures are the same as Fig. 4.2, precipitable water vapour above each station is set to $w = 2$ mm, and the instantaneous zenith coherence time is set $T_0 = 10$ s for both stations. Note that all tropospheric parameters are, however, independently set. The conversion from time delay to phase at 230 GHz is 1 rad = 0.7 ps.	32
4.4	The effect of residual troposphere phase noise on interferometric images of a point source observed for 12 hours at 230 GHz with 4 GHz bandwidth with the following array : SPT, ALMA, SMA, SMT, LMT and JCMT, assuming the same SEFDs as (author?) [26] and an elevation limit of 15°. For simplicity the weather parameters at each station were set to: coherence time $t_0 = 10$ sec; PWV depth $w = 1$ mm; ground pressure $P = 600$ mb; ground temperature $T = 273$ K. Top left: interferometric map with thermal noise only. Top right: atmospheric attenuation and sky noise (due to non-zero opacity) with 1% of the turbulent phase noise added. Bottom left: as previous but with 3% of turbulent phase contribution. Bottom right: as previous but with 6% turbulent phase contribution. The fractional turbulent phase contributions are illustrative of the effect of fringe-fitting errors. Note the decrease in the source peak flux with increasing turbulent tropospheric phase noise. Note further that the peak source centroid is offset from its true position (black crosshairs).	33
4.5	RMS relative amplitude error induced by pointing error with the 50 m (i.e. fully illuminated) LMT antenna as a function of pointing error offset ρ at 230 GHz. We assume that these errors are degenerate or non-separable from the self-calibration/fringe-fitting model used. See text for the description of the three models used. This simulation capability enables constraints on the magnitude of pointing-induced errors given a particular pointing calibration strategy.	34

List of Tables

2.1	A re-analysis of VLBI observations of Sgr A* by (author?) [39] has yielded revised estimates of the parameters associated with the Gaussian scattering kernel. An accurate estimation is needed for accurate extrapolation to 1.3 mm. Note that the position angle is measured East of North.	13
-----	--	----

Chapter 1

Introduction

Throughout the history of astronomy, we see celestial sources which appear point-like or unresolved with the instrumentation available at the time. To study these sources in enough detail to clarify their nature, ever more sophisticated instruments have to be developed.

These instruments span the electromagnetic spectrum, and here I recall several notable examples which illustrate the discovery potential of an increase in resolution.

At optical wavelengths, the Hubble Space Telescope was able to resolve the gravitational sphere of influence of the central supermassive black hole (SMBH) in nearby galaxies. These measurements uncovered the fundamental relations between black hole mass and both stellar bulge luminosities and velocity dispersions (Ferrasse and Merritt (2000), Gebhardt et al. (2000)) which has been a foundation for extra-galactic astronomy ever since.

A more recent example is a 2014 science verification result with the Atacama Large Millimetre Array (ALMA) [?] which resolves the molecular dust disk surrounding the young protostellar system, HL Tau Fig. 1.1. This observation showed, in unique detail, the orbit cleared out by forming planets which was surprising given that the stellar system was so young. The clarity of the image surpasses all previous work on the subject and provides a strong science case for conducting observations of similar systems with ALMA.

X-ray wavelengths with Chandra, we see the bullet cluster (Clowe 2004,)

The technique which achieves the highest resolution is Very Long Baseline Interferometry (VLBI)

VLBI is network

The development of VLBI, originated in the late 1960's with observations of compact, highly-variable objects, now known as quasars. Teams using VLBI discovered that these objects consist of core-jet systems. Also the presence of super-luminal jet motion. *TMS copy, paste : By using local oscillators at each antenna that are controlled by high-precision frequency standards, it is possible to preserve the coherence of the signals for time intervals long enough to measure interference fringes. The received signals are converted to an intermediate frequency low enough that they can be recorded directly on magnetic tape, and the tapes are subsequently brought together and played into a correlator.*

Examples of Arrays : Very Long Baseline Array (VLBA) : 1.4 - 87 GHz, European VLBI Network (EVN), African VLBI Network (AVN).

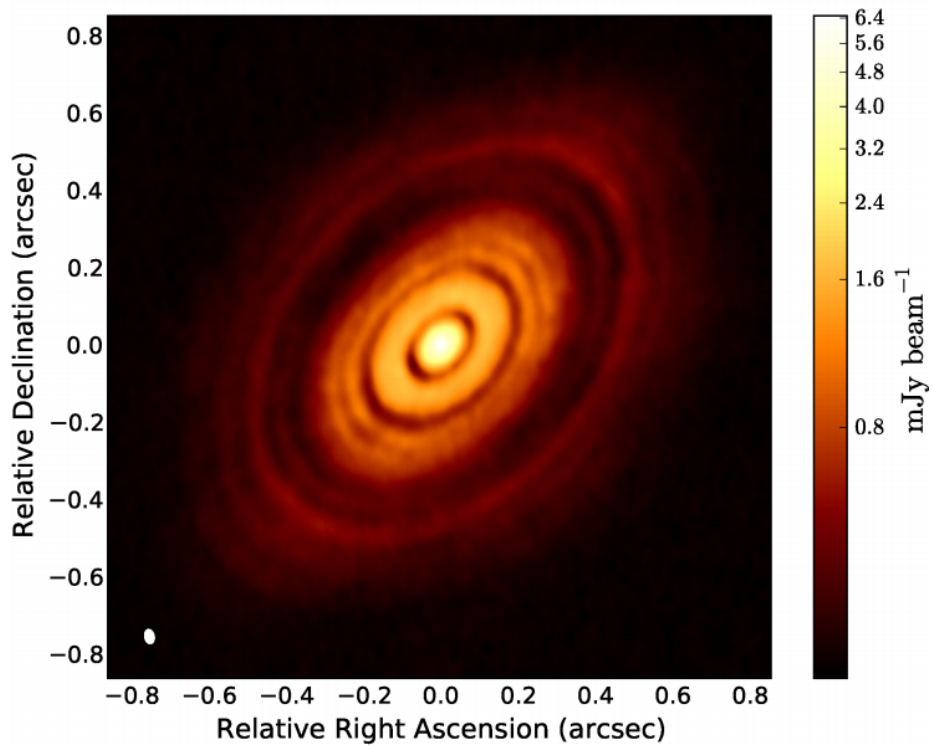


Figure 1.1: The young stellar system HL Tau, observed at 223 GHz by ALMA. The orbits of forming planets appear as dark rings cut out of the disk. The presence of these bodies are surprising given that host star is still very young. The detail in this image was made possible by the milliarcsec resolution achievable with ALMA.

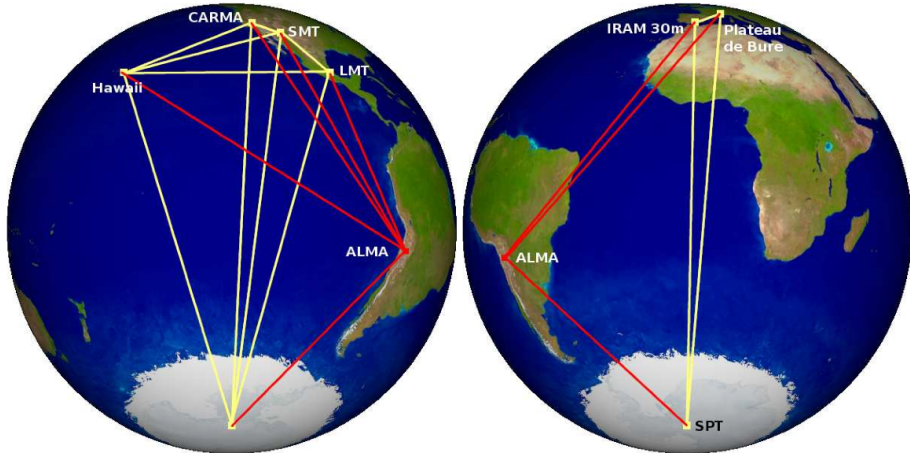


Figure 1.2: (Image credit: Remo Tilanius) Event Horizon Telescope uses **Earth-diameter baselines** to attain **resolution** $\sim 10 \mu\text{arcsec}$.

1.1 The Event Horizon Telescope (EHT)

This thesis is centred around such a class of emerging early 21st century instrumentation, known as Very Long Baseline Interferometry at millimetre wavelengths (mm-VLBI). This technique enables angular resolution on the order of $\sim 10 \mu\text{-arcsec}$ by maximising both antenna separation and observing frequency. The sub-field is being led by the Event Horizon Telescope consortium (EHT), an international project whose primary objective is to resolve the supermassive black holes (SMBH) located at the centre on our Galaxy, known as Sagittarius A* (Sgr A*), and M87 on angular scales comparable to the black hole event horizon. This thesis aims to contribute to the EHT objectives through algorithmic development of data simulation and parameter estimation pipelines, which are particularly relevant given the significant calibration challenges faced by the project.

1.1.1 Scientific opportunities

To constrain the physics near a black hole, the observation needs to be sensitive to scales comparable to the event horizon. For the case of a non-spinning or Schwarzschild black hole, the event horizon is spherically symmetric with a radius, $R_{\text{Sch}} = 2GM_{\text{BH}}/c^2$, where M_{BH} is the black hole mass, G is the gravitational constant and c is the speed of light. The angular size of such an event horizon in the far field approximation is $\theta_{\text{Sch}} = R_{\text{Sch}}/D \approx 0.02 \text{ nanoarcsec}$ (M_{BH}/M_{\odot})(kpc/ D) where D is the distance from observer to source. For SMBH's Sgr A* and M87, this results in $\theta_{\text{Sch}} \sim 5 - 10 \mu\text{-arcsec}$. The event horizon telescope will have baseline lengths $|b| \sim 10^3 \text{ km}$ and is currently observing at $\nu = 230 \text{ GHz}$, yielding a diffraction-limited angular resolution of $\theta_{\text{EHT}} = 1.22\nu/|b| \approx$. Hence EHT will be able to resolve these objects on the scale of the event horizon/gravitational radius.

Equally important to that the millimetre emission is optically thin and there-

fore probes inner emission region. The power spectrum of Sgr A* peaks in sub-mm bump. Synchtron emission. Lensed emission. the interferometric technique also filters out smooth mm emission.[Read Falke 1998]

FIG. basic grmhd image of black hole shadow, scale indicating resolution and eht beam size

Gravity as described by General Relativity (GR) has flawlessly agreed with all observational experiments, however GR has conceptual weaknesses, especially as it is not compatible with the quantum description of reality. Various alternatives to GR have been theorised which do not assume a purely classical description of matter. To test GR against its numerous alternatives, we have to observe gravity in the regime where we expect the largest observational deviations a GR prediction would have if it were only an approximate theory of gravity. The spacetime close to a SMBH is an ideal candidate, as the gravitational effects are very strong. Lensed emission of the gravitational lensed photon ring. The exact sizes and shapes of which indicate different spacetime and theories of gravity. Note that even in this regime, the deviation from GR is small. We can also explore black hole physics by testing the no-hair theorem or that black holes are only described by their mass, spin and charge by constraining the quadrupole moment of the black hole.deviations from the Kerr metric

FIG. Plot of analytic shapes and sizes of the bh shadow from the predictions of different theories of gravity

[AGN jet basics.]

Astrophysical jets were first discovered over a century ago, accretion onto a black hole was first postulated to power these jet byHowever a century later, the mechanism of accretion and jet launching ifrom SMBH are still highly debated.

Fig: Typical AGN jet illustration showing magnetic fields

Recently an industry of sophiscated General Relativistic Magneto-Hydrodyanic (GRMHD) simulations has developed yielding important insights but also new questions. Now, mm-VLBI has the opportunity of constrains the mechanisms. Specifically we can map the magnetic field configuration, which is a key aspect using polarimetry and Faraday Rotation. The quiescent and variability structure and also be explore in total intensity. Flaring structure. Distingush between accretion disk and inner jet. Distinguish between the different Jet and Disk models for each bh. Deterimine spin.

Fig: 2/3 panels of simulated images of disk and jet models of Sgr A*/M87

In M87, where the jet is dominant, micro-arcsecond scale astrometry, capable with the EHT, can determine the distance from the jet base from the event horizon, as well as the width of the jet base. Opening up new possibilities in explore particle production and other exotic physics occuring at the event horizon.

Fig: 2/3 panels of simulated polarimetric images of Sgr A*/M87 showing ordered magnetic fields

1.1.2 Challenges and obstacles

Performing Very Long Baseline Interferometry (VLBI) at mm-wavelengths presents unique calibration challenges, including very short atmospheric coherence times that are typically $\lesssim 10$ s [10], low calibrator source sky density, complex and variable calibrator source structure, and antenna pointing accuracies that are a non-negligible fraction of the antenna primary beam. These effects may place significant limitations on the sensitivity, image fidelity, and dynamic range that can be achieved with mm-VLBI. Performing mm-VLBI however, is a difficult task for a variety of reasons. Firstly the arrays are inhomogeneous, made up of a collection of different stations working together. Difficult to get time on all the stations. There are a variety of signal corruptions which take place. Briefly introduce signal corruptions, variability, ..etc, how these represent calibration and interpretation challenges.

1.1.3 Science extraction : parameter estimation and imaging

We need to measure the fractional asymmetry of the shadow shape with respect to its angular size to the few percent

Estimating the ‘macro’-parameters of Sgr A*, spin, orientation, position angle through a Bayesian parameter estimation analysis with closure quantities. Furthermore, unaccounted for systematic and/or non-Gaussian uncertainties could preclude robust, accurate Bayesian parameter estimation and model selection analyses of accretion flow [e.g. 6] and gravitational physics [e.g. ? 40], two of the EHT’s many objectives.

see psaltis 2015 for some other shadow detection criteria **Fig: A Broderick 2016 posterior probability distribution (?)**

1.2 Research questions and aims

1.3 A realistic mm-VLBI simulator

Given the significant observation challenges that the EHT faces, we have undertaken this project to build a mm-VLBI observation and signal corruption simulator. There are many benefits for using such a toolkit and indeed synthetic data simulation is common practice for every major scientific experiment. Two prominent examples is the extensive synthetic data generation for gravitational wave template matching for LIGO (ref) or for LHC particle collision experiments (ref). In essence such a simulator would fill in the final part of the theoretical signal propagation chain, effectively taking astrophysical simulations of the source (e.g. SMBH) as an input and returning realistic synthetic data. This allows a more effective interplay between theory and observation. The remainder of this section will briefly discuss several use cases for an EHT synthetic data simulator and how we have designed the software to meet these requirements.

A key observational use case is the testing of calibration, parameter estimation and imaging algorithms and strategies. As the inputs to the simulator

are known exactly, when passing simulated data through the data processing pipelines, we are better able to explore sources of error which are difficult to disentangle from intrinsic source features in real data. A straightforward way to perform such a test is through the creation of a set of ‘standard challenge’ dataset. Such datasets would be available to the entire community input into their calibration and/or imaging routines. Following this, a detailed comparison between the different strategies in varying regimes (source and other factors) can be made. Importantly, a systematic investigation of a particular algorithm across many different datasets could provide insight into subtle or previously unknown sources of error.

Bayesian parameter estimation and model selection analyses of accretion flow [e.g. 6] and gravitational physics [e.g. ? 40] offer a promising approach to constrain theoretical models when using visibilities or visibility derived quantities. However, unaccounted systematic errors in the signal processing chain could bias the posterior probability distribution, precluding a robust and accurate determination of key science parameters. Through the construction of an end-to-end simulation pipeline, the Bayesian parameter estimation procedure extended to handle more realistic synthetic data. This would entail combining many iterations data simulator with a solver to perform calibration and parameter estimation.

Simulated data can also assist in the optimisation of the experimental configuration. Financial constrains require the prioritisation of hardware upgrades e.g. increasing bandwidth, surface accuracy improvement, deployment of water vapour radiometers or additional receiver bands. Simulated data together with calibration and imaging pipelines can help to quantify the benefit of each improvement based on expected scientific return. This approach can even be extended to assess new candidate stations, especially as new geographic locations e.g. in Southern Africa are receiving increasing attention due to the potential long baselines to ALMA, SPT and European stations.

Recently, there has been an increase in the attention given to simulating EHT observations of Sgr A* ((author?) 16; (author?) 26; ?). However, these are primarily focused on image reconstruction and assume perfect phase calibration i.e. no troposphere-induced fringe-fitting errors; perfect antenna pointing accuracy; perfect phasing efficiency; and in most cases simple, non-variable Gaussian kernel smoothing to simulate ISM scattering. Clearly, as the EHT array is enhanced (and likely expanded), so too must the interferometric simulations evolve to provide ever-more realistic predictions on the confidence levels with which parameters can be extracted and hence exclude theoretical models of gravity and/or accretion flows.

Over the past decade, significant effort has been placed on advanced radio interferometric calibration and imaging algorithms for centimetre and metre-wave facilities in response to the large number of new arrays in construction or design phase (e.g. MeerKAT, ASKAP, SKA, LOFAR, HERA). A leading software package in this pursuit is MEQTREES¹ [36], which was developed to simulate, understand and address the calibration issues to be faced with the greatly enhanced sensitivity, instantaneous bandwidth, and field-of-view of such facilities. For example, MEQTREES is rooted in the Measurement Equation mathematical formalism [21], which parameterizes the signal path into distinct 2×2 complex

¹<https://ska-sa.github.io/meqtrees/>

matrices called Jones matrices. This formalism and applications thereof are laid out in [? ? ?] and are arbitrarily generalized to model any (linear) effect, including undesired signal corruptions that often may have subtle yet systematic effects. MEQTREES has been applied to correct for direction dependent calibration errors to JVLA and WSRT observations, achieving record-breaking high dynamic range images [?]. The effectiveness provided by the Measurement Equation formalism in radio interferometric calibration provides a strong motivation to explore its application to challenging goal of imaging a supermassive black hole silhouette with mm-VLBI. To construct this simulator we leverage off metre and cm-wavelength simulation and calibration successes and build a MEQTREES-based mm-VLBI-specific software package which we name, MEQSILHOUETTE. Use of MEQTREES and MEASUREMENT SET data format lends itself to investigating a range of different techniques that are used in other areas of interferometry (e.g. coh-Jones paper). While MEQTREES has not yet been used in the context of mm-wavelength observations, the framework is agnostic to higher frequency implementation as long as the Measurement Equation is appropriately constructed. This technology enables us to

1.4 Outline

Chapter 2

Theory

Our goal, is to add the final steps in the theory chain which transforms the GRMHD simulations into interferometric observables. For this to be achieved and for the theory higher up in the chain to be maximally useful in data interpretation, realistic signal corruptions need to be considered. Hence, the purpose of this module is to further the sophistication of the interplay between theory and observation in the field. The signal corruptions which we have identified as the most prominent occurs in the troposphere, interstellar medium (ISM) and within the stations themselves. First I will review some EM wave fundamental and introduce scattering theory, which is applicable to both the radiative process occurring in the troposphere and ISM. Following the general introduction I will explore each specific case.

2.1 Radio Interferometry

2.1.1 Measurement Equation

2.1.2 mm-VLBI observables and data products

If the visibility phase is highly variable as in the case of a turbulent atmosphere, conventional calibration and imaging techniques have severely limited (if any) success. However information can still be extracted from the raw visibilities in the form of closure quantities [32] or polarisation ratios [15]. Closure phase, defined as the sum of 3 visibility phases of a triangle of stations $\{i, j, k\}$, is a probe of asymmetry in source structure,

$$\Phi_{ijk} = \phi_{ij} + \phi_{jk} + \phi_{ki}. \quad (2.1)$$

Because most signal corruptions are station based, the gain phase terms $\phi_{ij} = \phi^{\text{true}} + \phi_i^G - \phi_j^G$ for each antenna will cancel, yielding a more robust observable.

The uncertainty on the closure phase is model dependent [42] and is given as a function of the SNR s of each baseline

$$u(\Phi_{ijk}) = \frac{\sqrt{4 + (s_{ij}s_{jk})^2 + (s_{jk}s_{ki})^2 + (s_{ij}s_{ki})^2 + 2(s_{ij}^2 + s_{jk}^2 + s_{ki}^2)}}{s_{ij}s_{jk}s_{ki}}, \quad (2.2)$$

where s_{ij} is defined as

$$s_{ij} = |V_{ij}| \sqrt{\frac{\tau \Delta\nu}{SEFD_i SEFD_j}}, \quad (2.3)$$

where τ is the vector averaging timescale, $\Delta\nu$ is the bandwidth, $|V_{ij}|$ is the visibility amplitude and $SEFD$ is the system equivalent flux density. The result that closure phase is entirely immune to station based effects breaks down however when time averaging in the presence of baseline dependent effects like thermal noise as illustrated in section ??.

2.1.3 Variability and the static source assumption

Implicit in our description of interferometry above, we assumed that the source remains approximately unchanged or static during the course of the observation. However, if this assumption does not hold (i.e. if the source is time-variable), the visibilities measured over the course of an observation can no longer be related to a single image and if they are, the resulting image would appear smeared out as it is averaged over many realisations. Note that I am using the term ‘variability’ in a general sense which refers to changes in any source observables. Most commonly variability is refers to changes in source flux (visibility amplitude) but I include changes in source structure and position (visibility phase) and source polarisation. Practically it is difficult to separate source and instrumental variability without accurate models and measurements for all non-source signal propagation effects. Although the static source assumption holds for most interferometric observations, the accretion flow and/or magnetic field structures around a SMBH can be variable on far shorter timescales. The primary mm-VLBI target, Sgr *, exhibits variability on timescales of minutes to hours in the radio (including in EHT observations), near-infrared (NIR), and X-ray bands [e.g. 2, 17, 47? , 14?]. This wealth of observational data has yielded several answers but the origin of the variability is still highly debated. To explain the observed delays between flares in different frequency bands, an expanding adiabatic plasma model (Marrone, 2008) has been presented however a recent flare observed with the EHT did not exhibit the increase in size expected from an expanding plasma outflow model [14]. Signatures of periodic variability at NIR and x-ray [?] have been used to argue for the presence of orbiting hotspots [10]. As the Innermost Stable Circular Orbit (ISCO) depends on spin of the BH, the spin can be constrain through the detection periodic orbital features. However a longer light curve in the NIR is more representative of a power-law scale variability [31]. These observations point to the possibility of multiple flaring mechanisms. An important mm-VLBI observational result is that variability in the polarisation domain is far more rapid than the total intensity (Johnson 2015b), indicating the presence of highly variable magnetic fields. In principle, the variability timescale can be comparable to the period of the Innermost Stable Circular Orbit (ISCO), which for Sgr A*, ranges from 4 minutes in the maximally rotating realisation to about half an hour for a non-rotating BH. The ISCO period for M87 is longer on the order of day scales. Considering light crossing times Δt_{cross} , we can estimate the angular size θ of the emission region to be of order $\theta \sim \Delta t_{\text{cross}} c / D_{\text{src}}$, where c is the speed of light and D_{src} is the observer-source distance. Hence for Sgr * at a distance of 8.3 kpc (Gillessen,

2009), for a flare of duration $\Delta t_{\text{cross}} = 10$ min, which corresponds to scales of $15R_{\text{Sch}}$, further evidence of emission areas close the event horizon. If a flare is dominated by a localised variable structure, several approaches [10? , 23] show that EHT can track flaring structures with $\sim 5 \mu\text{-arcsec}$ precision using closure quantities and polarimetric ratios which could help map the spacetime around the BH. Alternatively (**author?**) [28] show that a gaussian weighting scheme can be applied to mitigate the effects of variability and measure the quiescent structure although approach would downweight the longest baselines. However all of these approaches assume only gaussian thermal noise, gaussian-blurring in the ISM and no fringe-fitting errors.

2.2 Signal Corruptions

2.2.1 Scattering basics

Millimetre wavelength radiation originating at the Galactic Centre is repeatedly scattered along the signal path to the Earth-based observer. The first occurrence is due to electron plasma in the interstellar medium (ISM) ((**author?**) 5, (**author?**) 20), while the second is due to poorly-mixed water vapour in the Earth's troposphere ((**author?**) 7, (**author?**) 25). It is essential that the effects of the scattering phenomena are understood for a rigorous calibration and interpretation of data. Towards this end, simulation modules approximating scattering in both media are implemented in MEQSILHOUETTE. As an introduction to the separate descriptions of each, we review a simple scattering model.

An electro-magnetic wave is scattered when it passes through a medium with refractive index inhomogeneities. Following (**author?**) [33], this effect can be modeled as a thin screen, located between source and observer planes and orientated perpendicular to the line-of-sight. The screen, indexed by coordinate vector \mathbf{x} , adds a stochastic phase $\phi(\mathbf{x})$ to the incoming wave at each point on the screen, yielding a corrugated, outgoing wavefront. We define the Fresnel scale as $r_F = \sqrt{\lambda D_{\text{os}}/2\pi}$, where D_{os} is the observer-scatterer distance, or the distance where the geometrical path difference $\frac{2\pi}{\lambda}(D_{\text{os}} - \sqrt{D_{\text{os}}^2 + r_F^2}) = \frac{1}{2} \text{ rad}$.

To determine the resultant electric field at a point in the plane of the observer, indexed by coordinate vector \mathbf{X} , one has to take into account all possible ray paths from the screen to \mathbf{X} . To illustrate the model, a calculation of the scalar electric field generated by a point source, $\psi(\mathbf{X})$ yields the Fresnel-Kirchoff integral [3]

$$\psi(\mathbf{X}) = C \int_{\text{screen}} \exp \left[i\phi(\mathbf{x}) + i\frac{(\mathbf{x} - \mathbf{X})^2}{2r_F} \right] d\mathbf{x}, \quad (2.4)$$

where C is a numerical constant.

The statistics of $\phi(\mathbf{x})$ can be described by a power spectrum or equivalently the phase structure function,

$$D_\phi(\mathbf{x}, \mathbf{x}') = < [\phi(\mathbf{x} + \mathbf{x}') - \phi(\mathbf{x})]^2 >, \quad (2.5)$$

where \mathbf{x} and \mathbf{x}' represent two points on the screen and $<>$ denotes the ensemble average.

There is evidence that D_ϕ can be reasonably approximated by a power law dependence on the absolute distance r between points on the screen [1?]

$$D_\phi(r) = (r/r_0)^\beta, \quad r^2 = \mathbf{x}^2 - \mathbf{x}'^2 \quad (2.6)$$

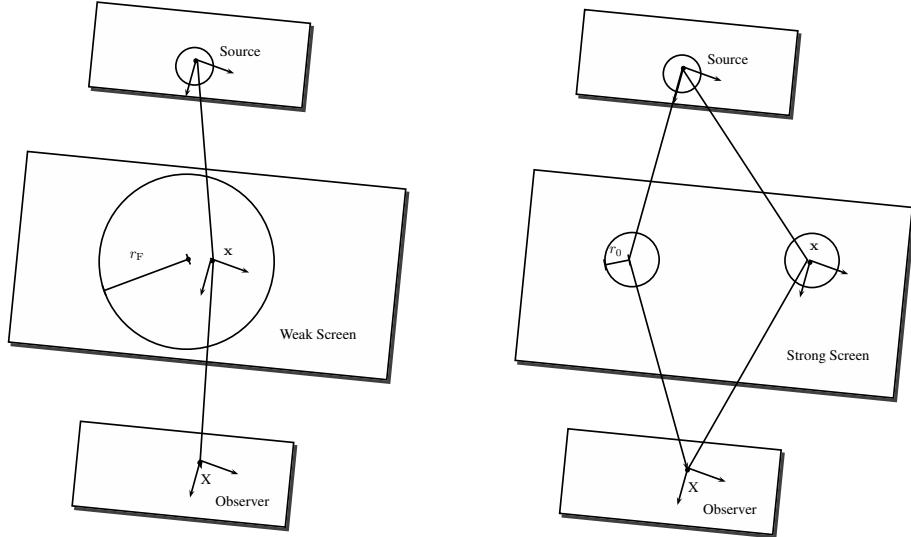


Figure 2.1: Illustration depicting the basics of scattering in the weak (left) and strong (right) regimes. In the weak regime, the signal is coherently propagated over an area, $A_{\text{weak}} \approx \pi r_F^2$ whereas in the strong regime, coherent propagation is split over many areas of size $A_{\text{strong}} \approx \pi r_0^2$.

where r_0 is the phase coherence length scale defined such that $D_\phi(r_0) = 1$ rad. Kolmogorov turbulence, which describes how kinetic energy injected at an outer length scale r_{out} cascades to increasingly smaller scales until finally dissipated at an inner length scale r_{in} , predicts $\beta = 5/3$ in the domain $r_{\text{in}} \ll r \ll r_{\text{out}}$. This scaling has been demonstrated to be a reasonable approximation for the ISM over scales $r \sim 10^2$ km to > 1 AU [?], and also for the troposphere with $r < \Delta h$, where Δh is the thickness of the turbulent layer [8]. The specifics of the tropospheric model will be explored further in later sections.

The two length scales, r_F and r_0 , define the nature of the scattering which is split into the strong and weak regimes, Fig. reffig:scatter. In weak scattering, $r_0 \gg r_F$ and hence by equation 2.6, $D_\phi(r_F) \ll 1$. This implies that most of the radiative power measured on a point \mathbf{X} will originate from a screen area $A_{\text{weak}} \approx \pi r_F^2$. Whereas in the regime of *strong scattering*, $r_0 \ll r_F$ yielding $D_\phi(r_F) \gg 1$. This results in coherent signal propagation onto the point \mathbf{X} from multiple disconnected zones each of area $A_{\text{strong}} \approx \pi r_0^2$ [33]. Scattering in the troposphere and ISM fall into the regimes of weak and strong scattering respectively.

To evolve the screen in time, we assume a frozen screen i.e. that the velocity of the individual turbulent eddies is dominated by the bulk motion of scattering medium [e.g. 25]. This allows us to treat the screen as frozen but advected over the observer by a constant motion. Hence time variability can be easily incorporated by the relative motion between source, scattering screen and observer.

Table 2.1: A re-analysis of VLBI observations of Sgr A* by (author?) [39] has yielded revised estimates of the parameters associated with the Gaussian scattering kernel. An accurate estimation is needed for accurate extrapolation to 1.3 mm. Note that the position angle is measured East of North.

major axis FWHM (mas/cm ⁻²)	1.32	0.04
minor axis FWHM (mas/cm ⁻²)	0.82	0.21
position angle (°)	77.8	9.7

2.2.2 Interstellar medium scattering

Electron density inhomogeneities in the interstellar medium (ISM) plasma scatter the radio emission from the Galactic centre. Radio interferometric observations of Sgr A* have characterised the basic properties of the intervening plasma material, however extensive developments in scattering theory and simulations have proved essential to the interpretation of more subtle scattering phenomena. This section begins with the early observational results which studied the Gaussian blurring effect of the scattering; we then expand on the scattering theory introduced in Sec. 2.2.1 to review the latest theoretical developments which explore the presence of scattering-induced substructure; finally we review recent observational results which account for scattering substructure in their data interpretation.

The dominant observational effect of the scattering for $\lambda \gtrsim$ cm is to convolve the intrinsic source structure with an elliptical Gaussian. The size of the Gaussian exhibits a λ^2 scaling dependence over several orders of magnitude [Fig. 2.2 ? 43, 5, 27], which is consistent with the wavelength dependence of the refractive index of a plasma. In order to determine the parameters of the scattering kernel, i.e. major axis, minor axis and position angle, one has to observe at wavelengths where the angular size of scattering ellipse is much larger than the expected source size. A Very Long Baseline Array (VLBA) + Green Bank Telescope (GBT) campaign [5] estimated the size at 1.31×0.64 mas cm⁻², oriented 78° east of north.

An accurate extrapolation of scattering kernel to 1.3 mm is important for the EHT scattering-mitigation strategy [16] which aims to deblur the scattered image through a deconvolution procedure. However as this extrapolation is over at least an order of magnitude, any small systematic error in the original measurement can significantly effect the 1.3 mm extrapolated parameters. A recent review of VLBI observations of Sgr A* [39] has noted that there are significant inconsistencies between different measurements. The authors used a Bayesian methodology to re-analyse the datasets resulting in increased uncertainties as shown in 2.1. The minor axis has a much larger uncertainty than the major axis due to the limited north-south coverage of the VLBA.

The Gaussian blurring effect can explained by the simple scattering model introduced in Sec. 2.2.1. Recall, that in the strong scattering regime light is propagated from coherent patches with linear size $\sim r_0$. Each patch will emit light coherently into a single-slit diffraction cone of angular size $\theta_{\text{scatt}} \sim \lambda/r_0$. An observer will hence be illuminated by many patches spanning θ_{scatt} , yielding a blurred and broadened image, with projected size on the screen equal to the *refractive scale*

$$r_{\text{ref}} = \theta_{\text{scatt}} D_{\text{os}} = r_F^2/r_0.$$

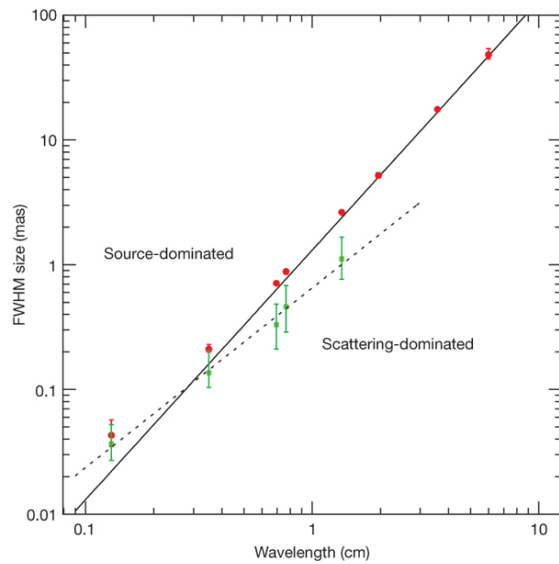


Figure 2.2: The λ^2 dependence of scattering kernel size is shown by the solid line. This has been derived from measurements made at $\lambda > 17$ cm [5]. The dotted line shows the derived intrinsic source size which scales as $\lambda^{1.44}$. This was derived from measurements in the wavelength range, $2 \text{ cm} < \lambda < 1.3 \text{ mm}$. The red circles show major-axis observed sizes of Sgr A* and the green points show the derived intrinsic major-axis size. This plot was reproduced from (author?) [12].

r_{ref} is the third fundamental length scale in the strong scattering regime and is associated with the refractive timescale,

$$t_{\text{ref}} = r_{\text{ref}}/v.$$

We can calculate r_0 given the FWHM of θ_{scatt} through the more precise relation

$$\theta_{\text{scatt}} = \frac{2\sqrt{2 \ln 2}}{2\pi} \lambda/r_0(M+1) \quad (2.7)$$

where $M = D_{\text{os}}/R$ is the magnification and R is the source-screen distance. The magnification factor is a correction to the model introduced in Sec. 2.2.1 when $R \sim \infty$ no longer holds and should be used when calculating distances in the observer plane [18]. The location of the scattering medium was originally thought to be quite close to Sgr A*. However, observations of a newly discovered pulsar, SGR J1745-29, indicate that the scattering screen is located at a distance $D_{\text{os}} = 5.8 \pm 0.3$ kpc, within the Scutum spiral arm. Using Eq. 2.7 and the parameters given in table 2.1, we find that the major axis of the coherence length at 1.3 mm, $r_0 \approx 3136.67$ km.

As the VLBI moves to higher frequencies, focus has shifted away from the well-studied Gaussian convolution effect of ISM scattering and onto the presence of stochastic scattering-induced substructure. To understand this phenomenon, we must first develop our conceptual framework.

Strong scattering can be further subdivided into *snapshot*, *average* and *ensemble-average* regimes [34, 18]. To understand the different regimes, remember that for each point on the source, the observer sees emission from coherent patches of size $\sim r_0$ spanning $\sim r_{\text{ref}}$. The diffraction cones from each of the patches will interfere, resulting in a multi-slit *diffractive scintillation* pattern.

In the *snapshot regime*, a compact source is observed with a narrow bandwidth and over a short time integration. This yields a single realisation of the diffractive scintillation pattern. By averaging over many snapshots, diffractive scintillation is quenched. This occurs if the source size θ_{src} is much larger than the diffractive scale $\theta_{\text{src}} \gg r_0/R$; if the fractional bandwidth $\delta\nu/\nu$ is much larger than the decorrelation bandwidth $\delta\nu/\nu \gg \delta\nu_{\text{dc}}/\nu \approx (r_0/r_F)^2$ [33]; or if the integration time t_{int} is much larger the diffractive timescale $t_{\text{int}} \gg t_0 = r_0/v$, where v is the relative velocity between screen, source and observer. This regime is hence only accessible through observations of compact objects like pulsars. On a side note, observations in this regime can be used to probe the source with angular resolution given by the $\sim \lambda/r_{\text{ref}}$ [e.g. 19]. This is because the scattering screen is essentially a lens of size $\approx r_{\text{ref}}$.

In the *average regime*, diffractive scintillation has been averaged over, however there still exists scintillation over scales comparable to the size of the scattered image of a point source $\sim r_{\text{ref}}$, termed *refractive scintillation*. Phase fluctuations on this scale acts like a weak lens to focus or defocus the λ/r_0 scale diffraction cones in the direction of the observer. For a point source this would lead to weak flux variations in the total flux [33]. We will show later that refractive scintillation leads to the presence of substructure for a resolved scatter-broadened source. In contrast to diffractive scintillation, refractive scintillation is much more difficult to average over. Typically the refractive time scale $t_{\text{ref}} = r_{\text{ref}}/v$ is on the order of weeks to months for Sgr A*; the fractional decorrelation bandwidth is on the order of unity $\delta\nu_{\text{dc}}/\nu \sim 1$; and the source has to be much larger than the image of a scattered point source $\theta_{\text{src}} \gg \theta_{\text{scatt}}$.

In the *ensemble-average regime*, both diffractive and refractive scintillation have been averaged over. It is in this regime when the scattering is equivalent to Gaussian convolution which is deterministic and not time variable.

A recent theoretical work [?] has derived a useful approximation of the resolved scattered image I_{ss} in the average regime,

$$I_{ss}(\mathbf{x}) \approx I_{src} (\mathbf{x} + r_F^2 \nabla \phi(\mathbf{x})), \quad (2.8)$$

where ∇ is the directional derivative. Here we have used the same two-dimensional coordinate system, indexed by \mathbf{x} to describe the source, screen and observer planes which are considered to be aligned along the vertical axis. The scattered image I_{ss} is approximated by a ‘reshuffling’ of the source image I_{src} . As $|\nabla \phi| \sim 1/r_0$, the magnitude of the translation of points on $I_{src} \sim r_{ref} \sim 10 \mu\text{-arcsec}$ in the case of Sgr A*.

Even though $\phi(\mathbf{x})$ is only coherent to $\sim r_0$, the directional phase derivative $\nabla \phi(\mathbf{x})$ remains spatially coherent over much larger scales. Following [?], the autocovariance of phase derivative can be related to the structure function

$$\langle [\partial_x \phi(\mathbf{x}_0)][\partial_x \phi(\mathbf{x}_0 + \mathbf{x})] \rangle = -\partial_x^2 \langle \phi(\mathbf{x}_0) \phi(\mathbf{x}_0 + \mathbf{x}) \rangle \quad (2.9)$$

$$= \partial_x^2 D_\phi(\mathbf{x}). \quad (2.10)$$

as $\langle \phi(\mathbf{x})^2 \rangle = 0$

Using a typical structure function [?], We are interested in the case $r_{in} \gg r_0$, the structure function becomes [?]

$$D_\phi = \begin{cases} \left(\frac{r}{r_0}\right)^2 & \text{if } r \ll r_{in}, \\ \frac{2}{\beta} \left(\frac{r_{in}}{r_0}\right)^{2-\beta} \left(\frac{r}{r_0}\right)^\beta & \text{if } r \gg r_{in}. \end{cases}$$

Note that the structure function is quadratic at small scales as fluctuations are smooth and then Kolmogorov then constant (Tatarskii, 1971). Hence We are interested in the case r/ggr_{in}

$$\partial_x^2 D_\phi(\mathbf{x}) = \left(\frac{r_{in}}{r_0}\right)^{2-\beta} 2(\beta-1) \frac{r^{\beta-2}}{r_0^\beta} \quad (2.11)$$

Therefore in the Kolmogorov regime $\beta = 5/3$, the coherence of image shift relative to the refractive scale $\propto (r/r_0)^{-1/3}$. Inner scale extends coherence and outer scale cuts it off.

If $\nabla \phi(\mathbf{x})$ was incoherent between patches of size $\sim r_0$, this would effectively be convolution with Gaussian of size r_{ref} .

A recent observation of Sgr A* at 3.5 mm by the VLBA+LMT [see Fig. ref:fig:substructure2 ?] show that the closure phase measured is consistent with refractive scintillation. Another observation at 1.3 cm shows flux modulation due to scattering substructure $\sim 10 \text{ mJy}$ [20] and other predictions show $\sim 60 \text{ mJy}$ for long East-West baselines and $\sim 25 \text{ mJy}$ for long North-South baselines [?], assuming a Gaussian source of $FWHM = 40 \mu\text{-arcsec}$.

Distinguishing intrinsic source structure and variability and ISM variability is an interesting challenge. Observations at mm-wavelengths have revealed deviations from the λ^2 scattering scaling law, see Fig. 2.2. This is interpreted as due to the presence of intrinsic source structure and has been fitted with a

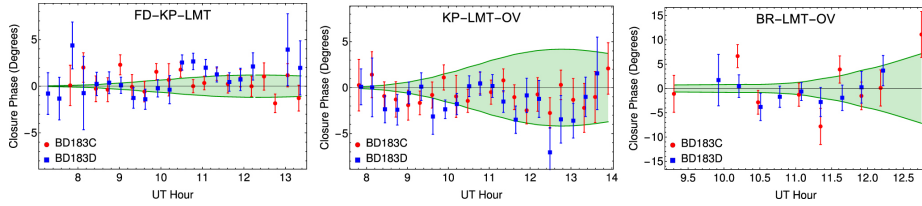


Figure 2.3: Closure phases recorded in a VLBA + LMT observation of Sgr A* at $\lambda = 3.5$ mm [?]. The data points are shown as red circles and blue squares and are only distinguished by the calibrator used. The green envelopes show the 1σ closure phase prediction induced by scattering-induced substructure. Reproduced from ?]

power-law with an exponent of 1.34 ± 0.01 [27]. This has enabled the constraint of various theoretical models [5], excluding advection-dominated accretion flows (ADAF) [?] and Bondi-Hoyle accretion [?]. However observations extending over month timescales are required to properly sample the larger scale inhomogeneities and even with multiple epoch observations, it can be difficult to distinguish source and scattering characteristics [29].

Knowledge of the scattering characteristics can allow the two to be decoupled without sampling a refractive ensemble. It therefore provides a robust and rapid mechanism for quantifying refractive effects.

2.2.3 Troposphere

The coherence and intensity of millimetre wavelength electromagnetic waves are most severely deteriorated in the lowest atmospheric layer, the troposphere which extends up to an altitude of $7 - 10$ km above sea level and down to a temperature $T \sim 218$ K [44]. The troposphere is composed of a number of different components including primary gases N₂ and O₂, trace gases e.g. water vapour and CO₂, as well as particulates of water droplets and dust. The rest of this section will explore the tropospheric corruption for the mm-VLBI case.

Propagation fundamentals

Consider a quasi-monochromatic wave passing through a linear medium,

$$E_\nu(x, t) = E_0 \exp^{i(kn_\nu x - 2\pi\nu t)}, \quad (2.12)$$

where $k = 2\pi\nu/c$ is the propagation constant in free space and $n = n_R + jn_I$ is the complex index of refraction. Note that we will occasionally omit the frequency dependence of n and related quantities to simplify the notation. If n_I is nonzero, the electric flux I will decay exponentially

$$I = EE^* = E_0^2 \exp(-\tau), \quad (2.13)$$

where τ is called the opacity or optical depth and is related to the absorption coefficient $\kappa = 4\pi\nu n_I/c$ via $d\tau = \kappa dx$. If $n_R > 1$ the phase velocity of light will decrease, $v_p = c/n_R$, which results in a time delay. The time delay, δt and

opacity τ can be calculated simultaneously,

$$\delta t + i\tau/4\pi\nu = 1/c \int_{path} d\mathbf{s} (n_\nu(\mathbf{s}) - 1). \quad (2.14)$$

Opacity and time delays are often viewed independently, however the electric field is real and causal and this imposes restrictions on the complex refractive index. Specifically n_R and n_I contain the same information and can be interchanged via the Kramers-Kronig relations.

Absorption is accompanied by emission and for a medium in local thermodynamic equilibrium, Kirchoff's law states that

$$\frac{\epsilon_\nu}{\kappa_\nu} = B_\nu(T), \quad (2.15)$$

where $\epsilon_\nu = dI_\nu/dx$ is the emission coefficient and $B_\nu(T)$ is the Planck function. Hence the absorbing molecules are also emitters, increasing system noise. Therefore opacity, time delay and atmospheric noise are interrelated and should be simulated consistently. On a side note this opens up the possibilities for phase calibration using measurements of sky emission via Water Vapour Radiometry (WVR).

Atmospheric corruptions in the (sub-)mm regime

An analysis of the absorption spectrum in the GHz range (Fig. 2.4), shows that it is dominated by transitions of H₂O and O₂ as well as a pseudo-continuum opacity which increases with frequency. The pseudo-continuum opacity is due to the cumulative effect of the far wings of a multitude of broadened water vapour lines above 1 THz [7]. At 230 GHz the absorption is typically 5 – 10% at the best sites, during good weather.

In contrast to the dry atmospheric components, water vapour mixes poorly and its time-variable spatial distribution induces rapid fluctuations in the time delays $\delta t(\nu)$ above each station. The phase error for a baseline (1,2) where antenna 1 is the reference will be

$$\delta\phi(t, \nu) = (\delta t_2(t, \nu) - \delta t_1(t, \nu))/\nu. \quad (2.16)$$

The water vapour column density is measured as the depth of the column when converted to the liquid phase and is referred to as the precipitable water vapour (PWV). PWV is directly proportional to the time delay and hence the phase delay,

$$\delta\phi \approx \frac{12.6\pi}{\lambda} \times w, \quad (2.17)$$

where w is the depth of the PWV column [7] and an atmospheric temperature $T = 270$ K has been assumed. This relationship between phase and water vapour content has been experimentally verified [22]. At 230 GHz, the change in PWV needed to offset the phase by 1 rad is $\Delta w \approx 0.03$ mm.

This sensitive dependence of phase coherence on atmospheric stability is aggravated by typically low antenna observation elevation angles as the atmospheric path length is increased; uncorrelated atmospheric variations between stations as correlated atmospheric variations fall away; and observing with a sparse VLBI array as this leads to less redundancy for calibration.

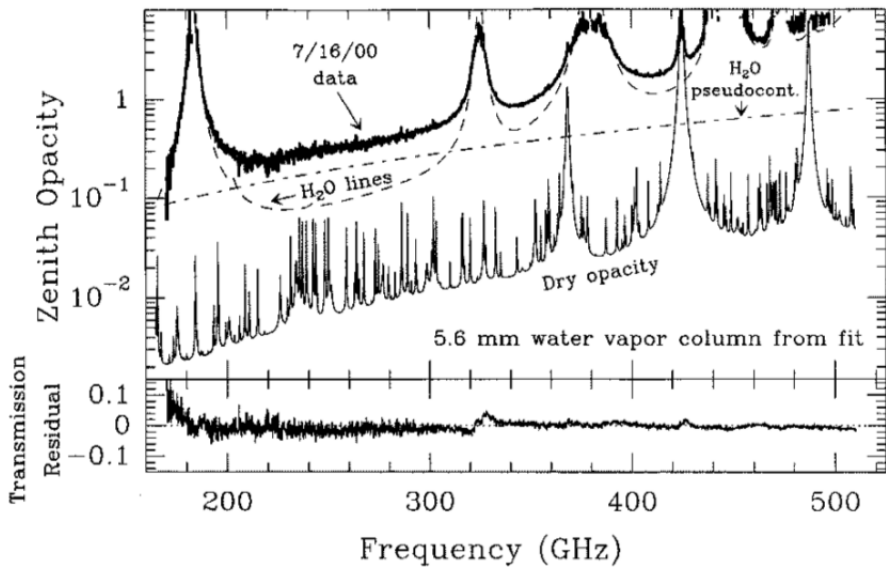


Figure 2.4: Recorded zenith absorption spectrum in the 160 – 520 GHz range, taken on Mauna Kea at an altitude of ~ 4000 m. The data has been fit to a sum of H₂O lines, an H₂O pseudo-continuum and dry absorption lines. The model has been generated using the ATM code, with the bottom panel showing the residuals. Here 'dry' refers to all atmospheric constituents except H₂O. Reproduced from (author?) [37]

Radiative transfer

The problem of radiative transfer through a static atmosphere is well described and implemented by the Atmospheric Transmission at Microwaves (ATM) code [37]. Here we provide a brief summary of the theory underpinning the package but see the original paper for further detail. ATM is commonly used in the Atacama Large Millimeter Array (ALMA) community [9, 35] and has been tested with atmospheric transmission spectra taken on Mauna Kea [?].

We start from the unpolarised radiative transfer equation, which is unidirectional in the absence of scattering,

$$\frac{dI_\nu(s)}{ds} = \epsilon_\nu(s) - \kappa_\nu(s)I_\nu(s), \quad (2.18)$$

where s is the coordinate along the signal path through the atmosphere. The assumption of local thermodynamic equilibrium (LTE) holds as the collisional timescale is much smaller than the time for spontaneous emission up to altitudes ≥ 80 km, after which there is only $\sim 0.001\%$ of mass left [37]. Applying 2.15, multiplying by $\exp(-\tau_\nu)$ and integrating from the top of the atmosphere ($s = 0$) yields,

$$I_\nu(s) = I_\nu(0)e^{-\tau_\nu(0,s)} + \int_0^s B_\nu(s')e^{-\tau_\nu(s',s)}\kappa_\nu(s')ds', \quad (2.19)$$

where s' is a dummy variable in the same direction as s and $\tau_\nu(0,s) = \int_0^s k_\nu(s')ds'$. $I_\nu(0)$ is normally taken as the radiance from the cosmic background. 2.19 will allow us to calculate the noise temperature of the atmosphere by converting the output radiance at the ground $I_\nu(s)$ to the equivalent blackbody temperature through inversion the Planck function. To calculate the opacity and complete the above integral, κ_ν needs to be calculated over the frequency range. The time delay δt can be calculated using the Kramers-Kronig relations.

A general equation for the absorption coefficient for a transition between a lower l and upper u states is given in the original paper. Here we merely point out that it should be proportional to the energy of the photon, $h\nu_{l \rightarrow u}$, the transition probability or Einstein coefficient, $B_{l \rightarrow u}$, the line-shape, $f(\nu, \nu_{l \rightarrow u})$ and the number densities N of electronic populations. Line profiles which describe pressure broadening (perturbations to the Hamiltonian due to the presence of nearby molecules) and Doppler broadening are used. The condition of detailed balance further requires that decays from the upper state are included yielding, $g_u B_{u \rightarrow l} = g_l B_{l \rightarrow u}$, where g is the degeneracy of the electronic state. Putting this together we find,

$$\kappa(\nu)_{l \rightarrow u} \propto h\nu B_{l \rightarrow u} \left(\frac{N_l}{g_l} - \frac{N_u}{g_u} \right) f(\nu, \nu_{l \rightarrow u}), \quad (2.20)$$

where the Einstein coefficients are calculated from the inner product of the initial and final states with the dipole transition operator,

$$B_{l \rightarrow u} = \frac{2\pi}{3\hbar^2} | \langle u | \mu | l \rangle |^2, \quad (2.21)$$

where $|u\rangle, |l\rangle, |\mu\rangle$ are the wavefunctions of upper and lower states and the dipole transition operator respectively. The number densities of the two states,

N_u and N_l in local thermodynamic equilibrium (LTE) are simply related to the local number density and temperature via Boltzmann statistics,

$$\frac{N_n}{N} = g_n \frac{\exp -\frac{E_n}{kT}}{Q} \quad (2.22)$$

where Q is the partition function. $Q = \sum_i g_i \exp -E_i/kT$.

Physically, the lineshape originates from perturbations to the hamiltonian due to proximity to neighbouring molecules, called pressure broadening, and at lower pressures, thermal doppler broadening. A Van Vleck -Weisskopf (VVW) profile is used for pressure broadening. At lower pressures this is convolved with a gaussian which arises from the Maxwellian distribution.

Transition lines at radio wavelengths result from rotational state transitions. To calculate the inner product given in equation 2.21, hamiltonians for linearly symmetric rotors (e.g. O_2 , CO) and asymmetric rotors are used. The asymmetric rotations are decomposed into three principal rotation axes with differing rotational constants governing each axis. Rotational constants were measured by the authors as well as drawn from a variety of literature. Partition functions and transition probability are calculated using approximations taken from the literature.

Far wing broadening of H_2O lines > 1.2 THz extends to lower frequencies and is not completely represented by the VVW profile. This is believed to be due to self-self collisions of water molecules. Additionally there are terms from the dry atmosphere related to transient dipoles and Debye absorption which are not represented in the lineshape. To correct for these effects two pseudocontinua are used, which take the form of a power law dependence on frequency, temperature and the molecular densities.

Turbulent phase fluctuations

Visibility phase instability $\delta\phi(t)$ due to tropospheric turbulence is a fundamental limitation to producing high fidelity, science-quality maps with a mm-VLBI array [44]. The coherence time-scale is typically too rapid ($\lesssim 10$ s) for fast switching calibration, so other calibration procedures (e.g. water vapour radiometry, paired antennas, and/or self-calibration) must be performed. Self-calibration is the most commonly used but is limited by the integration time needed to obtain adequate SNR to fringe fit. Phase decoherence often leads to the use of closure quantities to perform model fitting [11, 4, 43].

At centimeter wavelengths and below, water vapour in the troposphere dominates errors in delay rate over hydrogen maser clock errors. Stochastic phase errors lead to a decrease in measured flux due to incoherent vector averaging. This makes it difficult to obtain adequate SNR for calibration. The uncertainty in the phase degrades structural information which makes conventional imaging difficult and hence closure quantities are often used (e.g. Fish et al 2011). Incoherent phases represent a fundamental limit to all types of interferometry.

Following from section 2.2.1, we can model the statistics of $\delta\phi(t)$ with a thin, frozen, Kolomogorov-turbulent phase screen moving with a bulk velocity, v . We set the height h of the screen at the water vapour scale height of 2 km above ground. We will show later that the thickness Δh of the atmospheric turbulent layer can be neglected in our implementation. At 1.3 mm, the Fresnel scale is $r_F \approx 0.45$ m and experiments show annual variations of $r_0 \sim 50 - 500$ m above

Mauna Kea [30] and $r_0 \sim 90 - 700$ m above Chajnantor [41], where both sites are considered to have excellent atmospheric conditions for millimetre astronomy. As $r_F < r_0$, this is an example of weak scattering.

The required field-of-view (FoV) of a global mm-VLBI array is typically $\text{FoV} < 1$ mas or $\sim 10 \mu\text{m}$ at a height of 2 km, which is roughly 7-8 orders of magnitude smaller than the tropospheric coherence length. The tropospheric corruption can therefore be considered constant across the FoV and, from the perspective of the Measurement Equation, modeled as a diagonal Jones matrix per time and frequency interval. As VLBI baselines are much longer than the coherence length, $|\mathbf{b}| \geq 1000$ km $\gg r_0$, the phase screen at each site must be simulated independently.

Our aim then is to produce a phase error time sequence $\{\delta\phi(t_i)\}$ for each station which is added to the visibility phase. We invoke the frozen screen assumption and write the structure function as a function of time, $D(t) = D(r)|_{r=vt}$. The temporal structure function $D(t)$ provides an efficient route to sample the variability of the troposphere at the typical integration time of the dataset, $t_{\text{int}} \sim 1$ sec.

The temporal variance of the phase is a function of the temporal structure function, and accounting for time integration yields [see 45, B3]

$$\sigma_\phi^2(t_{\text{int}}) = (1/t_{\text{int}})^2 \int_0^{t_{\text{int}}} (t_{\text{int}} - t) D_\phi(t) dt. \quad (2.23)$$

Assuming power-law turbulence and integrating yields,

$$\sigma_\phi^2(t_{\text{int}}) = \left[\frac{1}{\sin \theta(\beta^2 + 3\beta + 2)} \right] \left(\frac{t_{\text{int}}}{t_0} \right)^\beta, \quad (2.24)$$

where $t_0 = r_0/v$ is the coherence time when observing at zenith and $1/\sin \theta$ is the approximate airmass which arises as $D_\phi \propto w$. As $r \ll \Delta h$, where Δh is the thickness of the turbulent layer, a thin screen exponent of $\beta = 5/3$ is justified [45]. The phase error time-series takes the form of a Gaussian random walk per antenna. At mm-wavelengths, the spectrum of water vapour is non-dispersive up to a few percent [9] and so we can assume a simple linear scaling across the bandwidth.

Phase fluctuations $\delta\phi(t)$ can also be simulated by taking the inverse Fourier transform of the spatial phase power spectrum. However this approach is much more computationally expensive, e.g. for an observation length t_{obs} involving $N_{\text{ant}} = 8$ independent antennae with dish radii $r_{\text{dish}} = 15$ m, wind speed $v = 10 \text{ m s}^{-1}$ and pixel size equal to r_F , the number of pixels $N_{\text{pix}} \approx N_{\text{ant}} t_{\text{obs}} r_{\text{dish}}^2 / (v r_F^3) \sim 10^8$. Additionally, due to fractal nature of ideal Kolmogorov turbulence, the power spectrum becomes unbounded as the wavenumber approaches zero which makes it difficult to determine the sampling interval of the spatial power spectrum [24].

2.2.4 Instrumental

Thermal Noise

The level of thermal noise in the data will define the sensitivity of the interferometer to detect a source and also to distinguish fine source characteristics.

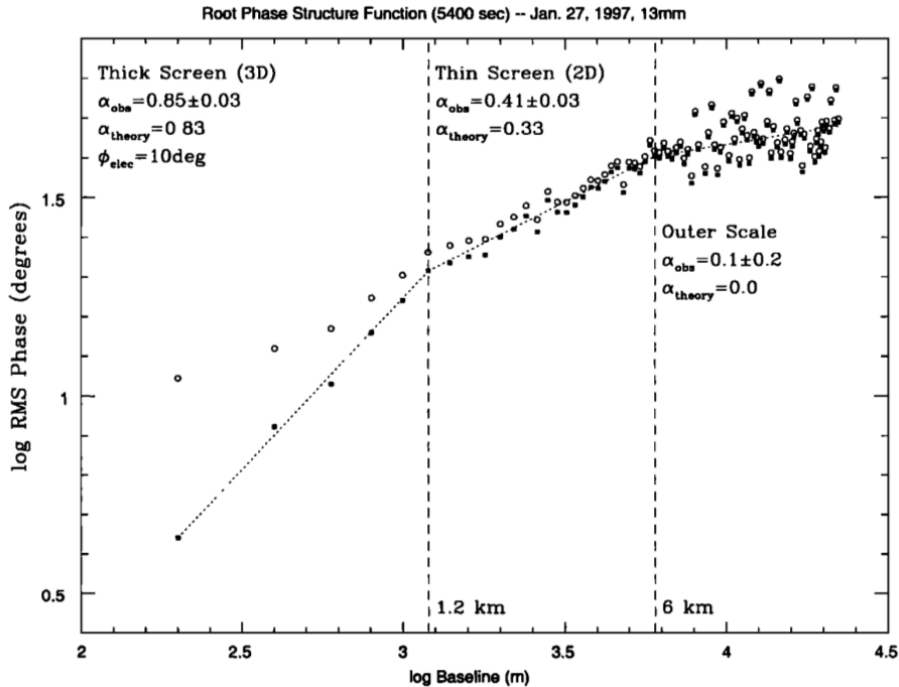


Figure 2.5: RMS visibility phase variations versus baseline length for an observation of 1-Jy celestial calibrator 0748 + 240 with VLA in BnA configuration at 22 GHz for 90 min. The open circles show the rms phase as measured whereas the solid squares show these same values with a constant noise term of 10 subtracted in quadrature. showing β changes with distance on the phase screen. Note the three distinct regime but continuous variation in between. The three regimes of the root phase structure function as predicted by Kolomogorov turbulence theory are indicated. Reproduced from [?]

Closure quantities are especially prone to high levels of thermal as multiple visibilities are combined. A derivation of the thermal noise of an interferometer can be made through derivation of the thermal noise of an antenna and then correlating the result [46]. The RMS thermal noise of an interferometer $\{i, j\}$ over a bandwidth $\Delta\nu$ and an integration time is given by

$$\Delta S_{ij} = \frac{1}{\eta_s} \sqrt{\frac{SEFD_i SEFD_j}{2\Delta\nu t_{int}}}, \quad (2.25)$$

where η_s is the system efficiency and $2\Delta\nu t_{int}$ is the number of independent samples. The $SEFD$ is a measure of the sensitivity of an antenna, accounting for the efficiency, collecting area and thermal noise and is defined as the flux density of a source with the same power,

$$SEFD = 2k_B T_{sys}/(\eta_a A), \quad (2.26)$$

where A is the antenna area, η_a is the antenna efficiency, T_{sys} is the system temperature and the factor $\frac{1}{2}$ accounts for only sampling 1 polarisation.

Antenna Pointing

All antennas suffer pointing errors to some degree due to a variety of factors including dish flexure due to gravity, wind and thermal loading, as well as drive mechanics. This corresponds to an offset primary beam, which should only translate to minor amplitude errors if the pointing error θ_{PE} is significantly smaller than the primary beam (i.e. $\theta_{PE} \ll \theta_{PB}$). In the Measurement Equation formalism, this offset can be represented by a modified (shifted) primary beam pattern in the E -Jones term

$$\mathbf{E}_p(l, m) = \mathbf{E}(l_0 + \delta l_p, m_0 + \delta m_p), \quad (2.27)$$

where $\delta l_p, \delta m_p$ correspond to the directional cosine offsets. This could be a problem for millimetre observations as the primary beam is significant, e.g. for a 30 m dish at 1.3 mm, $\theta_{PB} \sim 10$ arcsec, compared to the pointing error which is on the order of arcseconds. A standard beam model which we will make use of later is the analytic WSRT beam model [38]

$$E(l, m) = \cos^3(C\nu\rho), \quad \rho = \sqrt{\delta l_p^2 + \delta m_p^2} \quad (2.28)$$

where C is a constant, with value $C \approx 130$ GHz $^{-1}$. Note that the power beam EE^H becomes \cos^6 .

An antenna tracking a source will suffer a slow, continuous time-variable pointing error associated with the tracking error σ_{track} . Physically this could be attributed to changes in wind, thermal and gravitational loading which all change with telescope pointing direction and over the course of a typical few hour observation. Using the MeqTrees software package, such behaviour has been demonstrated to occur with the Westerbork Synthesis Radio Telescope (WSRT, [?])¹.

Whilst a stationary phase centre is tracked, the pointing error should evolve slowly and smoothly, however, in mm-VLBI observations the phase centre is

¹See also <https://indico.skatelescope.org/event/171/session/9/contribution/20>

often shifted to another source/calibrator. This would cause the pointing error to change abruptly, with an absolute pointing error $\sim \sigma_{\text{abs}}$. Source/calibrator change is scheduled every 5-10 minutes in a typical millimetre observation. The point is that even though EHT will be able to determine the pointing offset when observing a calibrator with well known structure, when the antennas slew back to a source (e.g. Sgr A*) with less certain or variable source structure, the pointing error could change significantly. This is exacerbated by the scarcity of mm-wavelength calibrators, which are often widely separated from the source.

Polarisation leakage

2.3 A primer on calibration and imaging

Chapter 3

Software implementation

3.1 Design objectives

Our primary aim is to test and research mm-VLBI calibration, imaging and parameter estimation algorithms/strategies through the construction of a synthetic data simulation framework. To address the many questions within the wide scope of this objective, one must be able to setup and run a diversity of experiments within the simulation framework. This places definite constraints on the software architecture. In particular, the framework should

- enable the implementation of all relevant classes of signal corruption within a formalism which ensures consistency with the causal signal transmission chain,
- be compatible with time-variable GRMHD source models which are to be used as inputs,
- be organised in modularised structure so that it is flexible, extendable and could be incorporated by other interferometric algorithms e.g. a calibration or a parameter estimation algorithm,
- The modular structure should also enable the construction and execution of arbitrary observations.

3.2 Architechture and Workflow

In this section, we will review how the architechural design and workflow of the simulator architechture has been designed to meet the above objectives. To fulfill the first objective, we try to cast signal corruptions in the RIME formalism (see section 2.1.1), and where this is not possible, to fit those particular signal corruptions into the causally correct position in the signal transmission chain, with proper consider given to non-communitivity of elements in the signal transmission path. The implementation of each signal corruption is described in the following subsections. The remaining objectives fall into the realm of software design and will be discussed in this subsection.

We have chosen to write the high level simulation code using the `PYTHON` language. `PYTHON` is a general purpose language, is geared towards readability,

and is well supported by a comprehensive library and wide user base (including astronomers). Specifically PYTHON interfaces well with a modern interferometric toolbox, MEQTREES, as well as our data formats of choice: FITS for image cubes and the MEASUREMENT SET¹ MS for visibilities. Although the higher level functionality is written in PYTHON, the bulk of the computational load (MS and visibility generation) is called through the faster C++ language. We use MS as our data format as it is directly accessible via the PYRAP library and is the data format used by MEQTREES which performs the visibility generation and pointing error simulation. Although in the mm-VLBI subfield other data formats are currently still more popular than the MS, i.e. UVFITS or IOFITS, with the completion of ALMA, the MS format should become the next modern data format and already is used at the Joint Institute for VLBI in Europe (JIVE).

To create a flexible and modular structure, the software implementation is divided into essentially 2 parts:

- an object-oriented framework which contains all the building blocks to control the logic of each individual step in the signal propagation chain,
- a driver script which initialises the most abstract class in the framework with the required inputs and determines the propagation chain describing that particular pipeline.

The conceptual flow diagram of one realisation of a MEQSILHOUETTE simulation pipeline is shown in Fig. 3.1. To emphasise the framework is not restricted to this sequence of operations and allows for the exact pipeline to be quite general. This flexibility is made possible through the use of *Object-Orientation*, which will be elaborated on later.

All inputs to the simulator are specified by a configuration file, containing a dictionary, which is the sole input to the driver script. This dictionary contains everything needed by the pipeline to determine the particular observation configuration (frequency, bandwidth, start time, etc), which signal corruption implementation should be employed and where the sky model and antenna table are located in the filesystem.

The sky model is typically a time-ordered list of FITS images, where each image represents the source total intensity over a time interval $\Delta t_{\text{src}} = t_{\text{obs}}/N_{\text{src}}$, where t_{obs} is the observation length and N_{src} is the number of source images. Currently the pipeline only supports total intensity. ²parametric source model consisting of Gaussians or point sources.

Antenna table is in the CASA format, and can readily be created or altered using the PYRAP library.

The primary outputs of the pipeline are an interferometric dataset in MS format along with the closure phases and uncertainties and a dirty and/or deconvolved image (or spectral cube if desired. The modular structure of the pipeline allows for imaging and deconvolution algorithms to be employed. There exists a CASA task for conversion to UVFITS. As the pipeline is easily flexible other data products can be easily produced as needed e.g. polarisation ratios or time-frequency averaged data.

A major step is to create a comprehensive MS which can handle arbitrary scans lengths and start times as well as arbitrary frequency channelisation and

¹<https://casa.nrao.edu/Memos/229.html>

²Later versions of MEQSILHOUETTE will enable the full Stokes cubes as input.

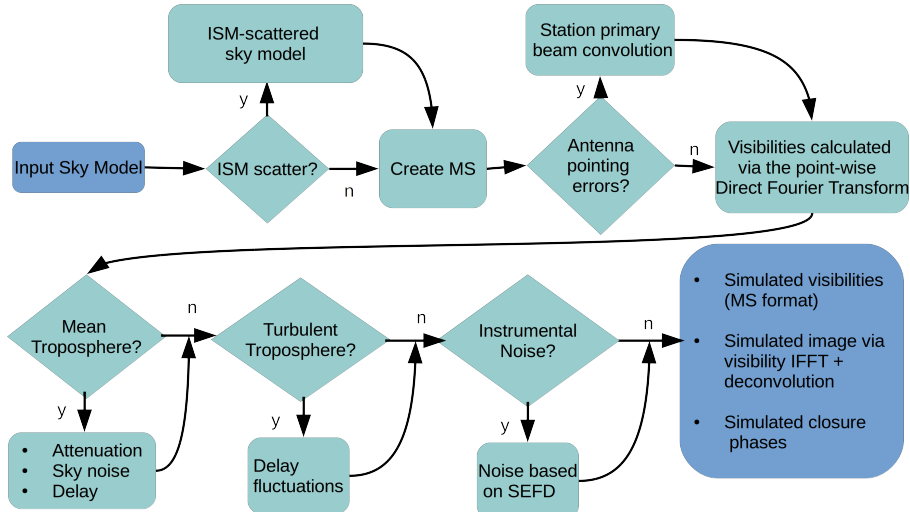


Figure 3.1: Flow diagram showing basic sequence of a MEQ-SILHOUETTE simulation pipeline. The specific sequence is determined by the driver script. The details of the station information, observation strategy, tropospheric and ISM conditions are specified in a user-defined input configuration file. The pipeline is extendable, allowing any additional, arbitrary Jones matrices to be incorporated.

bandwidth. This is performed using the SIMMS³ tool. SIMMS provides an easy to use interface to construct general MS, given an appropriate antenna table, which can be created manually using the PYRAP library.

In order to make the framework as clean and modular as possible we have made extensive use of object orientation. The first major class, *SimpleMS*, was intended to abstract and modularise the MS and MS-only derived attributes (e.g. visibility data and station positions) and methods (e.g. functions to calculate station elevations and closure phases) as well as expose these attributes and methods more efficiently than following PYRAP procedures which become verbose when used frequently.

The second MS-related class, *TropMS*, handles the calculations relevant to tropospheric and thermal noise corruptions. This class is a child of *SimpleMS* and is initialised with weather and station information. Note that a child contains all the methods and attributes of its parent. This allows the tropospheric corruption implementation to use, whilst being separated from, the core MS functionality. The details of the tropospheric corruption is provided in subsection 3.2.2.

The third MS-related class is the *SimCoordinator*, and it is a child of the *TropMS* class. *SimCoordinator* is designed to make arbitrary simulations easy and efficient to construct and execute on a high level. It is the only MS class directly initialised in the driver script and hence the low level functionality and attributes of its parents are abstracted from the user. In addition to inher-

³<https://github.com/radio-astro/simms>

ited functionality, *SimCoordinator* can call the ISM-scattering task (see subsection 3.2.1), and MEQTREES functionality of visibilities and simulation of antenna pointing errors using the MEQTREES : TURBO-SIM task, where the visibilities are calculated through evaluation of the Fourier Transform at each UVW coordinate in the dataset, the time and frequency resolution of which is specified by the user.

3.2.1 ISM scattering

As described in section ??, ISM scattering towards Sgr A* falls into the *average regime*, wherein diffractive scintillation is averaged out but refractive scintillation is still present. As mm-VLBI observations can resolve the scatter-broadened image of Sgr A*, an implementation of scattering is needed which approximates the subtle changes in its extended source structure. Such an approximation has been implemented in the PYTHON-based SCATTERBRANE⁴ package, and is based on ?]. The algorithm generates a phase screen based on the two dimensional spatial power spectrum [see ?, Appendix C] which incorporates inner and outer turbulent lengths scales and then implements 2.8 using an interpolation function modified by the phase screen.

SCATTERBRANE allows variation in all parameters associated with the scattering screen which is essential as aspects of the scattering towards the galactic centre is still unconstrained.

We include the SCATTERBRANE software, which has already yielded important context for mm-VLBI observations towards Sgr A* [e.g. ?], within the MEQSILHOUETTE framework. Our ISM module interfaces the SCATTERBRANE code within an interferometric simulation pipeline. This module enables simultaneous use of time-variable ISM scattering and time-variable intrinsic source structure within a single framework. The user is able to select a range of options relating to the time-resolution and epoch interpolation/averaging of both. By default, if the time resolution chosen to sample the source variability Δt_{src} and screen variability Δt_{ism} are unequal, we set

- $\Delta t_{\text{ism}} = \Delta t_{\text{src}}$ if $\Delta t_{\text{src}} < \Delta t_{\text{ism}}$
- $\Delta t_{\text{ism}} = R(\frac{\Delta t_{\text{src}}}{\Delta t_{\text{ism}}})\Delta t_{\text{src}}$ if $\Delta t_{\text{src}} > \Delta t_{\text{ism}},$

where R rounds the fraction to the nearest integer. This modification to the ISM sampling resolution avoids interpolation between different snapshots of the intrinsic source structure.

3.2.2 Atmospheric corruption simulator

3.2.3 Pointing error simulator

3.3 RODRIGUES interface

For community use, we host the online, RODRIGUES, interface, found at <http://rodrigues.meqtrees.net/>. Each of the components of the simulator run in Docker containers. **Looks like the infrastructure is going to change, re: discussions with Gijs and Sphe, so going to wait before writing this.

⁴<http://krosenfeld.github.io/scatterbrane>

Chapter 4

Results and analysis

4.1 Canonical simulations

Tropospheric induced closure phase errors !!A bug which came from averaging

In this paper, we present the first release of the MEQSILHOUETTE synthetic data simulation package. The pipeline is optimised towards mm-VLBI, taking into account user-specified stages of the signal propagation path, which enables the quantification of a range of systematic effects. Focus has been placed on modeling the effects of signal transmission through the ISM and troposphere as well as instrumental errors (i.e. pointing error and thermal noise). Time variability in all relevant domains (source, array, ISM, troposphere) is implemented. The run time for a typical simulation with a realistic instrumental setup is on the order of minutes. Implementation of polarisation effects is intended in the next release.

The ISM scattering implementation SCATTERBRANE, based on ?], has been incorporated into the pipeline. Fig. 4.1 provides an example of closure phase and flux variability over a 4 day period using a static source. Accurate simulation of the ISM-induced closure phase variation is essential in order to make any inference on asymmetric, event-horizon scale structure [e.g. 13?]. This will become even more important as the EHT sensitivity increases by an order of magnitude in the near future. Note that if the source has intrinsic spatial variability as in the case of a hotspot model [10], this will increase ISM variability as the relative motion between source, screen and observer is increased.

In section ??, we show how antenna pointing errors of the LMT could introduce fractional RMS amplitude variations $\sigma_{\Delta V/V_0} \leq 0.4$ on the timescale of phase centre switching. This would occur if the calibrator is widely separated from the source, as is often the case in mm-VLBI. In contrast tracking errors are less problematic with $\sigma_{\Delta V/V_0} \leq 0.05$. If the gain error is non-separable from the calibration model used, it could be interpreted as intrinsic variability, substructure and/or increased noise. If unaccounted for, this effect has the potential to limit the dynamic range of mm-VLBI images. Further tests to constrain the pointing uncertainties of EHT stations will lead to more accurate interferometric simulations and hence the overall impact on black hole shadow parameter estimation. Here we demonstrate the capability to incorporate a range of plausible pointing error effects into a full simulation pipeline.

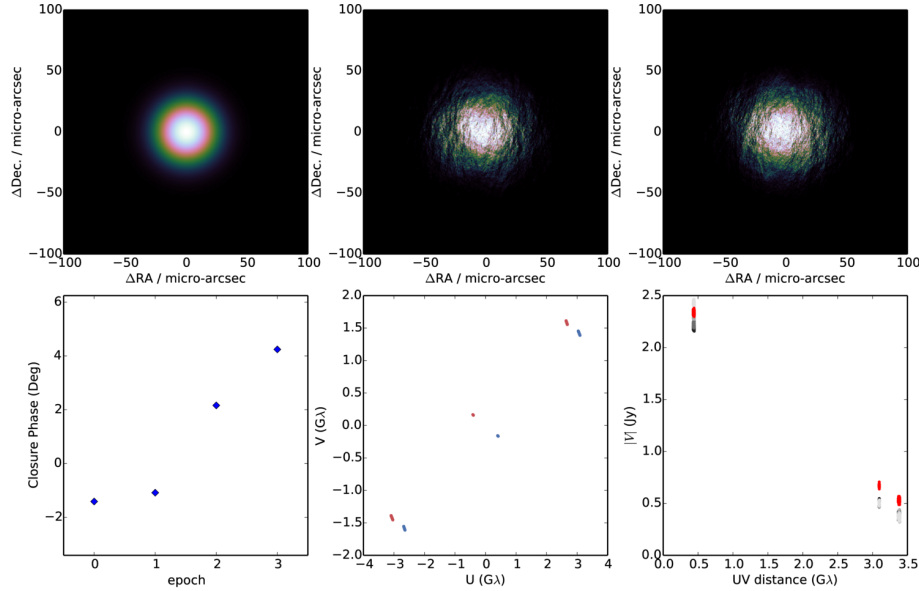


Figure 4.1: An example simulation of ISM scattering towards Sgr A*. The top panel, left to right, shows the original $\text{FWHM} = 40 \mu\text{-arcsec}$ Gaussian (**top left**), the ISM scattered image on the first night (**top middle**) and last night (**top right**) of the observation respectively. The bottom panel, left to right, shows the evolution of the 10 minute-averaged closure phase with epoch (**bottom left**), *uv*-tracks for any particular night (**bottom middle**) and the visibility amplitudes $|V|$ of the unscattered (red) and scattered (grey-scale) sources as a function of *uv*-distance (**bottom right**). Variations of the flux on the shortest baselines reveal total flux modulation while flux variations $\Delta|V|$ on longer baselines and non-zero closure phases track the fluctuations in refractive noise. When compared to the latest published observations of Sgr A* [13], we see that the observed and simulated closure phase variability are consistent. Furthermore, ISM scattering simulations can constrain the variability fraction associated with the screen, enabling a more robust estimation of source variability.

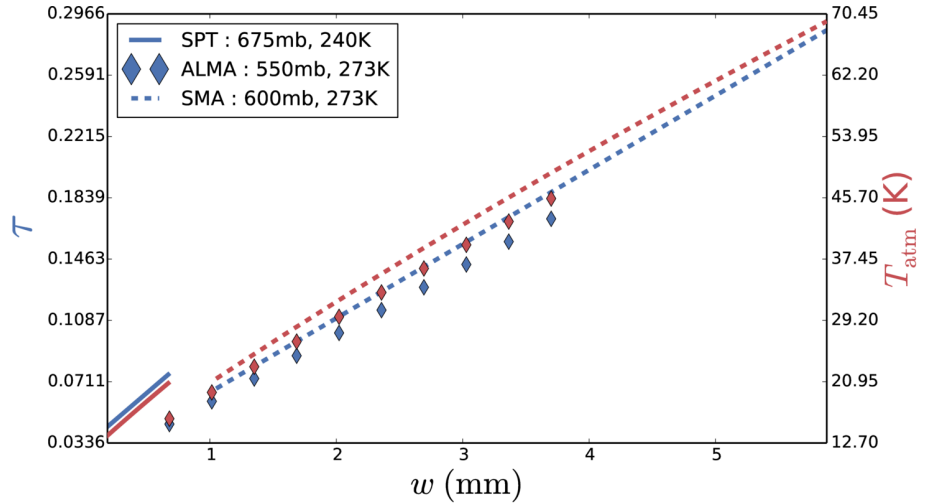


Figure 4.2: Best fit opacity (red) and sky brightness temperature (blue) line solutions at $\nu = 230$ GHz as a function of precipitable water vapour (PWV) for three indicative ground pressures and temperatures which approximately represent the sites of SPT (solid), ALMA (diamond) and SMA (dashed). The legend shows the estimated input ground (pressure, temperature) parameters for each site.

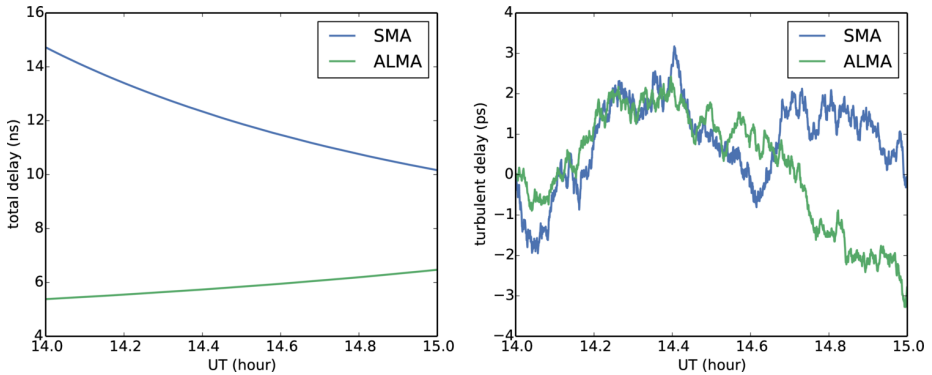


Figure 4.3: Simulation of the total delay (left) and the turbulent atmospheric delay (right) for SMA (blue) and ALMA (green) sites towards Sgr A*. Ground pressures and temperatures are the same as Fig. 4.2, precipitable water vapour above each station is set to $w = 2$ mm, and the instantaneous zenith coherence time is set $T_0 = 10$ s for both stations. Note that all tropospheric parameters are, however, independently set. The conversion from time delay to phase at 230 GHz is 1 rad = 0.7 ps.

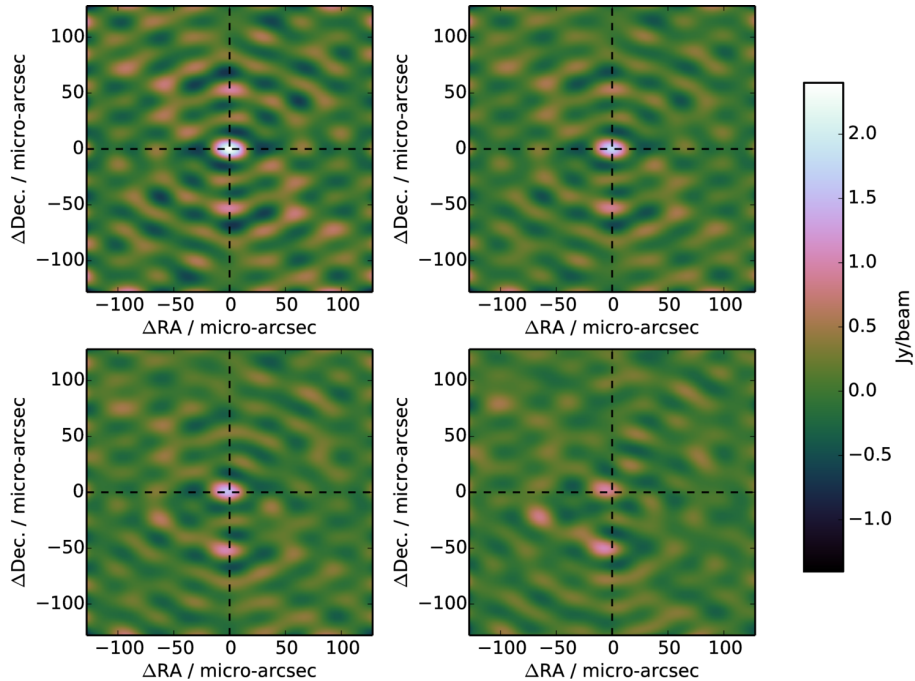


Figure 4.4: The effect of residual troposphere phase noise on interferometric images of a point source observed for 12 hours at 230 GHz with 4 GHz bandwidth with the following array : SPT, ALMA, SMA, SMT, LMT and JCMT, assuming the same SEFDs as (**author?**) [26] and an elevation limit of 15° . For simplicity the weather parameters at each station were set to: coherence time $t_0 = 10$ sec; PWV depth $w = 1$ mm; ground pressure $P = 600$ mb; ground temperature $T = 273$ K. **Top left:** interferometric map with thermal noise only. **Top right:** atmospheric attenuation and sky noise (due to non-zero opacity) with 1% of the turbulent phase noise added. **Bottom left:** as previous but with 3% of turbulent phase contribution. **Bottom right:** as previous but with 6% turbulent phase contribution. The fractional turbulent phase contributions are illustrative of the effect of fringe-fitting errors. Note the decrease in the source peak flux with increasing turbulent tropospheric phase noise. Note further that the peak source centroid is offset from its true position (black crosshairs).

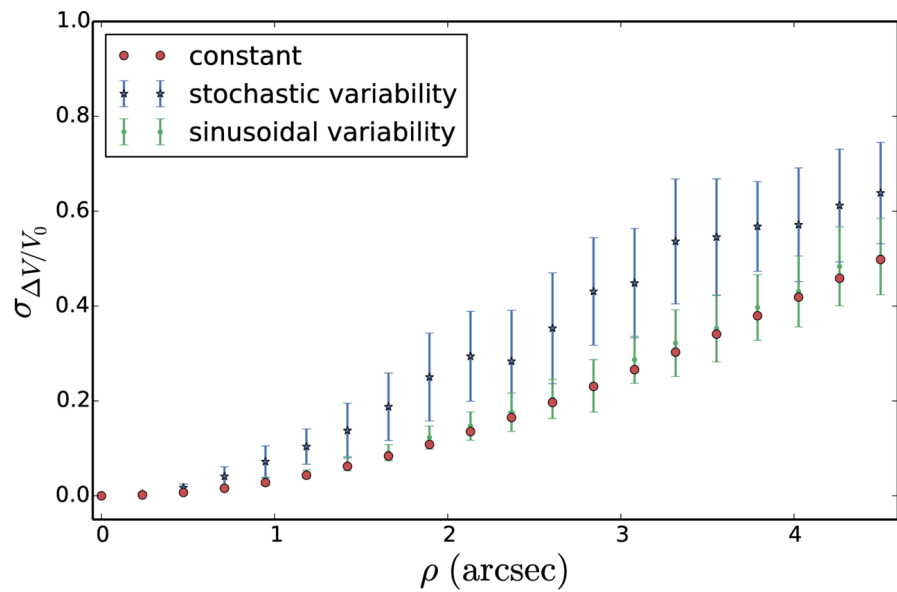


Figure 4.5: RMS relative amplitude error induced by pointing error with the 50 m (i.e. fully illuminated) LMT antenna as a function of pointing error offset at 230 GHz. We assume that these errors are degenerate or non-separable from the self-calibration/fringe-fitting model used. See text for the description of the three models used. This simulation capability enables constraints on the magnitude of pointing-induced errors given a particular pointing calibration strategy.

In section ?? we explore the observational consequences of observing through a turbulent troposphere. In this simulation, we assume a simple point source model and apply increasing levels of turbulence-induced phase fluctuations before imaging using the two dimensional inverse fast Fourier transforms. We note a rapid attenuation in peak flux due to incoherent averaging, slight offsets in the source centroid and the presence of spurious imaging artefacts. Surprisingly, in this configuration, there was no evidence of blurring or a loss of resolution with the uncertainties. In an upcoming paper, we perform a systematic exploration of the turbulent tropospheric effects on the accuracy of fringe-fitting algorithms/strategies, through use of an automated calibration procedure and including the added complexity of a time-variable source.

Significant progress has been made in the theoretical and numerical modeling of the inner accretion flow and jet launch regions near a supermassive black hole event horizon. With MEQSILHOUETTE, we now have the ability to couple these with sophisticated interferometric and signal propagation simulations. This offers a tool to enable a more closely-knit and effective interplay between theoretical predictions and observational capabilities. Moreover, detailed interferometric simulations will enable us to quantify systematic effects on the black hole and/or accretion flow parameter estimation.

4.2 A comparison to real data

4.3 Calibration and imaging of a time variable source in the presence of the troposphere

Later versions of MEQSILHOUETTE will enable the full Stokes cubes as input. This should not entail much work as our chosen data formats (MS, FITS) and the simulator in MEQTREES already support full stokes logic. Signal propagation through the ISM and troposphere as well as antenna based complex gains errors are polarisation independent. The work would be primarily involve altering the existing scripts to dealing with the extra dimension in the FITS files i.e. book keeping.

Chapter 5

Conclusion

In light of the science objectives of mm-VLBI observations and software advances in the broader radio interferometry community, a mm-VLBI data simulator has been developed. An important feature is that this simulation pipeline is performed using the MEASUREMENT SET format, in line with ALMA and future VLBI data formats. The focus has been placed on simulating realistic data given an arbitrary theoretical sky model. To this end, the simulator includes signal corruptions in the interstellar medium (ISM), troposphere and instrumentation. Examples of typical corruptions have been demonstrated, which show that each corruption can significantly affect the inferred scientific parameters. Particular focus has been placed on EHT observations, however, the pipeline is completely general with respect to observation configuration and source structure. Time variability in all domains (source, array, ISM, troposphere) is implemented. Future releases of MEQSILHOUETTE will include polarisation dependent corruptions. The creation of a close interface between sophisticated theoretical and interferometric mm-VLBI simulations will enhance the scientific opportunities possible with the EHT.

Bibliography

- [1] J. W. Armstrong, B. J. Rickett, and S. R. Spangler. Electron density power spectrum in the local interstellar medium. , 443:209–221, April 1995.
- [2] F. K. Baganoff, M. W. Bautz, W. N. Brandt, G. Chartas, E. D. Feigelson, G. P. Garmire, Y. Maeda, M. Morris, G. R. Ricker, L. K. Townsley, and F. Walter. Rapid X-ray flaring from the direction of the supermassive black hole at the Galactic Centre. , 413:45–48, September 2001.
- [3] M. Born and E. Wolf. Principles of Optics Electromagnetic Theory of Propagation, Interference and Diffraction of Light. 1980.
- [4] G. C. Bower, H. Falcke, R. M. Herrnstein, J.-H. Zhao, W. M. Goss, and D. C. Backer. Detection of the Intrinsic Size of Sagittarius A* Through Closure Amplitude Imaging. *Science*, 304:704–708, April 2004.
- [5] G. C. Bower, W. M. Goss, H. Falcke, D. C. Backer, and Y. Lithwick. The Intrinsic Size of Sagittarius A* from 0.35 to 6 cm. , 648:L127–L130, September 2006.
- [6] A. E. Broderick, V. L. Fish, M. D. Johnson, K. Rosenfeld, C. Wang, S. S. Doeleman, K. Akiyama, T. Johannsen, and A. L. Roy. Modeling Seven Years of Event Horizon Telescope Observations with Radiatively Inefficient Accretion Flow Models. , 820:137, April 2016.
- [7] C. L. Carilli and M. A. Holdaway. Tropospheric phase calibration in millimeter interferometry. *Radio Science*, 34:817–840, 1999.
- [8] C. E. Coulman. Fundamental and applied aspects of astronomical 'seeing'. , 23:19–57, 1985.
- [9] E. I. Curtis, B. Nikolic, J. S. Richer, and J. R. Pardo. Atmospheric dispersion and the implications for phase calibration. *ArXiv e-prints*, December 2009.
- [10] S. S. Doeleman, V. L. Fish, A. E. Broderick, A. Loeb, and A. E. E. Rogers. Detecting Flaring Structures in Sagittarius A* with High-Frequency VLBI. , 695:59–74, April 2009.
- [11] S. S. Doeleman, Z.-Q. Shen, A. E. E. Rogers, G. C. Bower, M. C. H. Wright, J. H. Zhao, D. C. Backer, J. W. Crowley, R. W. Freund, P. T. P. Ho, K. Y. Lo, and D. P. Woody. Structure of Sagittarius A* at 86 GHZ using VLBI Closure Quantities. , 121:2610–2617, May 2001.

- [12] S. S. Doeleman, J. Weintraub, A. E. E. Rogers, R. Plambeck, R. Freund, R. P. J. Tilanus, P. Friberg, L. M. Ziurys, J. M. Moran, B. Corey, K. H. Young, D. L. Smythe, M. Titus, D. P. Marrone, R. J. Cappallo, D. C.-J. Bock, G. C. Bower, R. Chamberlin, G. R. Davis, T. P. Krichbaum, J. Lamb, H. Maness, A. E. Niell, A. Roy, P. Strittmatter, D. Werthimer, A. R. Whitney, and D. Woody. Event-horizon-scale structure in the supermassive black hole candidate at the Galactic Centre. , 455:78–80, September 2008.
- [13] V. L. Fish, K. Akiyama, K. L. Bouman, A. A. Chael, M. D. Johnson, S. S. Doeleman, L. Blackburn, J. F. C. Wardle, W. T. Freeman, and the Event Horizon Telescope Collaboration. Observing—and Imaging—Active Galactic Nuclei with the Event Horizon Telescope. *ArXiv e-prints*, July 2016.
- [14] V. L. Fish, S. S. Doeleman, C. Beaudoin, R. Blundell, D. E. Bolin, G. C. Bower, R. Chamberlin, R. Freund, P. Friberg, M. A. Gurwell, M. Honma, M. Inoue, T. P. Krichbaum, J. Lamb, D. P. Marrone, J. M. Moran, T. Oyama, R. Plambeck, R. Primiani, A. E. E. Rogers, D. L. Smythe, J. SooHoo, P. Strittmatter, R. P. J. Tilanus, M. Titus, J. Weintraub, M. Wright, D. Woody, K. H. Young, and L. M. Ziurys. 1.3 mm Wavelength VLBI of Sagittarius A*: Detection of Time-variable Emission on Event Horizon Scales. , 727:L36, February 2011.
- [15] V. L. Fish, S. S. Doeleman, A. E. Broderick, A. Loeb, and A. E. E. Rogers. Detecting Changing Polarization Structures in Sagittarius A* with High Frequency VLBI. , 706:1353–1363, December 2009.
- [16] V. L. Fish, M. D. Johnson, R.-S. Lu, S. S. Doeleman, K. L. Bouman, D. Zoran, W. T. Freeman, D. Psaltis, R. Narayan, V. Pankratius, A. E. Broderick, C. R. Gwinn, and L. E. Vertatschitsch. Imaging an Event Horizon: Mitigation of Scattering toward Sagittarius A*. , 795:134, November 2014.
- [17] R. Genzel, R. Schödel, T. Ott, A. Eckart, T. Alexander, F. Lacombe, D. Rouan, and B. Aschenbach. Near-infrared flares from accreting gas around the supermassive black hole at the Galactic Centre. , 425:934–937, October 2003.
- [18] J. Goodman and R. Narayan. The Shape of a Scatter Broadened Image - Part Two - Interferometric Visibilities. , 238:995, June 1989.
- [19] C. R. Gwinn, M. D. Johnson, J. E. Reynolds, D. L. Jauncey, A. K. Tzioumis, H. Hirabayashi, H. Kobayashi, Y. Murata, P. G. Edwards, S. Dougherty, B. Carlson, D. del Rizzo, J. F. H. Quick, C. S. Flanagan, and P. M. McCulloch. Size of the Vela Pulsar’s Emission Region at 18 cm Wavelength. , 758:7, October 2012.
- [20] C. R. Gwinn, Y. Y. Kovalev, M. D. Johnson, and V. A. Soglasnov. Discovery of Substructure in the Scatter-broadened Image of Sgr A*. , 794:L14, October 2014.
- [21] J. P. Hamaker, J. D. Bregman, and R. J. Sault. Understanding radio polarimetry. I. Mathematical foundations. , 117:137–147, May 1996.

- [22] D. C. Hogg, F. O. Guiraud, and M. T. Decker. Measurement of excess radio transmission length on earth-space paths. , 95:304–307, March 1981.
- [23] M. D. Johnson, V. L. Fish, S. S. Doeleman, A. E. Broderick, J. F. C. Wardle, and D. P. Marrone. Relative Astrometry of Compact Flaring Structures in Sgr A* with Polarimetric Very Long Baseline Interferometry. , 794:150, October 2014.
- [24] R. G. Lane, A. Glindemann, and J. C. Dainty. Simulation of a Kolmogorov phase screen. *Waves in Random Media*, 2:209–224, July 1992.
- [25] O. P. Lay. The temporal power spectrum of atmospheric fluctuations due to water vapor. , 122, May 1997.
- [26] R.-S. Lu, A. E. Broderick, F. Baron, J. D. Monnier, V. L. Fish, S. S. Doeleman, and V. Pankratius. Imaging the Supermassive Black Hole Shadow and Jet Base of M87 with the Event Horizon Telescope. , 788:120, June 2014.
- [27] R.-S. Lu, T. P. Krichbaum, A. Eckart, S. König, D. Kunneriath, G. Witzel, A. Witzel, and J. A. Zensus. Multiwavelength VLBI observations of Sagittarius A*. , 525:A76, January 2011.
- [28] R.-S. Lu, F. Roelofs, V. L. Fish, H. Shiokawa, S. S. Doeleman, C. F. Gamme, H. Falcke, T. P. Krichbaum, and J. A. Zensus. Imaging an Event Horizon: Mitigation of Source Variability of Sagittarius A*. , 817:173, February 2016.
- [29] J.-P. Macquart and G. C. Bower. Understanding the Radio Variability of Sagittarius A*. , 641:302–318, April 2006.
- [30] C. R. Masson. Atmospheric Effects and Calibrations. 59:87–95, 1994.
- [31] L. Meyer, T. Do, A. Ghez, M. R. Morris, G. Witzel, A. Eckart, G. Bélanger, and R. Schödel. A 600 Minute Near-Infrared Light Curve of Sagittarius A*. , 688:L17, November 2008.
- [32] J. D. Monnier. Phases in interferometry. , 51:604–616, October 2007.
- [33] R. Narayan. The Physics of Pulsar Scintillation. *Philosophical Transactions of the Royal Society of London Series A*, 341:151–165, October 1992.
- [34] R. Narayan and J. Goodman. The shape of a scatter-broadened image. I - Numerical simulations and physical principles. , 238:963–1028, June 1989.
- [35] B. Nikolic, R. C. Bolton, S. F. Graves, R. E. Hills, and J. S. Richer. Phase correction for ALMA with 183 GHz water vapour radiometers. , 552:A104, April 2013.
- [36] J. E. Noordam and O. M. Smirnov. The MeqTrees software system and its use for third-generation calibration of radio interferometers. , 524:A61, December 2010.
- [37] J. R. Pardo, J. Cernicharo, and E. Serabyn. Atmospheric transmission at microwaves (ATM): an improved model for millimeter/submillimeter applications. *IEEE Transactions on Antennas and Propagation*, 49:1683–1694, December 2001.

- [38] A. Popping and R. Braun. The standing wave phenomenon in radio telescopes. Frequency modulation of the WSRT primary beam. , 479:903–913, March 2008.
- [39] D. Psaltis, F. Öznel, C.-K. Chan, and D. P. Marrone. A General Relativistic Null Hypothesis Test with Event Horizon Telescope Observations of the Black Hole Shadow in Sgr A*. , 814:115, December 2015.
- [40] D. Psaltis, N. Wex, and M. Kramer. A Quantitative Test of the No-hair Theorem with Sgr A* Using Stars, Pulsars, and the Event Horizon Telescope. , 818:121, February 2016.
- [41] S. J. Radford and M. A. Holdaway. Atmospheric conditions at a site for submillimeter-wavelength astronomy. 3357:486–494, July 1998.
- [42] A. E. E. Rogers, S. S. Doeleman, and J. M. Moran. Fringe detection methods for very long baseline arrays. , 109:1391–1401, March 1995.
- [43] Z.-Q. Shen, K. Y. Lo, M.-C. Liang, P. T. P. Ho, and J.-H. Zhao. A size of \sim 1AU for the radio source Sgr A* at the centre of the Milky Way. , 438:62–64, November 2005.
- [44] A. R. Thompson, J. M. Moran, and G. W. Swenson, Jr. Interferometry and Synthesis in Radio Astronomy, 2nd Edition. 2001.
- [45] R. N. Treuhaft and G. E. Lanyi. The effect of the dynamic wet troposphere on radio interferometric measurements. *Radio Science*, 22:251–265, April 1987.
- [46] J. M. Wrobel and R. C. Walker. Sensitivity. 180:171, 1999.
- [47] F. Yusef-Zadeh, D. Roberts, M. Wardle, C. O. Heinke, and G. C. Bower. Flaring Activity of Sagittarius A* at 43 and 22 GHz: Evidence for Expanding Hot Plasma. , 650:189–194, October 2006.